9047 - 17

NACA TN 2677

TECH LIBRARY KAFB, NM
0065457

NATIONAL ADVISORY COMMITTEE FOR AERONAUTICS

TECHNICAL NOTE 2677

WING-BODY INTERFERENCE AT SUPERSONIC SPEEDS WITH AN APPLICATION TO COMBINATIONS WITH RECTANGULAR WINGS

By Jack N. Nielsen and William C. Pitts

Ames Aeronautical Laboratory
Moffett Field, Calif.

Washington
April 1952

AFMDC
TECHNICAL LIBRARY
AFL 2811
PERMANENT
RECORD

319.98/41

TECH LIBRARY KAFB, NM

0065457

NATIONAL ADVISORY COMMITTEE FOR AERONAUTICS

TECHNICAL NOTE 2677

WING-BODY INTERFERENCE AT SUPERSONIC SPEEDS WITH AN APPLICATION TO COMBINATIONS WITH RECTANGULAR WINGS

By Jack N. Nielsen and William C. Pitts

SUMMARY

An exact theoretical method is developed that permits the determination of the pressure field of a wing-body combination having a circular body and a wing with supersonic leading and trailing edges. Detailed calculations have been performed for wing-body combinations composed of rectangular wings mounted at incidence on bodies at zero angle of attack for effective chord-radius ratios of 4 or less. For large effective chord-radius ratios some asymptotic results have been obtained. It was determined that for the family of combinations having an effective chord-radius ratio of 4 the area of the wing blanketed by the body does not generate any lift itself but rather acts to support the lift generated by the exposed wing, and that the body is less than 50 percent effective in reflecting lift back to the wing. For chord-radius ratios less than 4, the relative amount of reflection increases.

The significant fact was determined that for rectangular wing-body combinations for which the effective chord-radius ratio is greater than 4, most of the loss of lift due to interference can be estimated from the first term of the Fourier series used in the analysis. This fact was used to determine asymptotic lift results for the region where no exact calculations were made. The asymptotic expressions, together with the calculations, allowed the construction of design charts showing the lift and center-of-pressure location of the exposed wing panels as a function of effective aspect ratio and effective chord-radius ratio. The charts show that as a result of interference the lift on the exposed wing panels in combination with the body can be reduced as much as 15 percent below the value for the wing panels joined together, and that the center of pressure of the exposed wing panels can move forward as much as 4 percent of the wing chord.

INTRODUCTION

In recent years the problems of supersonic wing-body interference have occupied the attention of many workers in aerodynamics. The large amount of effort expended on the subject is a result of the important effects that interference can have on the over-all aerodynamic characteristics of wing-body combinations. The trend toward using large bodies and small wings at supersonic speeds, especially for missiles, is the prime reason for the increased importance of wing-body interference at these speeds.

Much significant work has already been done in the field. In reference 1, Spreiter has shown that, when a wing-body combination is slender in the sense of his paper, simple expressions for the lift and moment coefficients can be derived. These results were obtained by reducing a three-dimensional problem for the wave equation to a two-dimensional problem for Laplace's equation. Another approach is that of simplifying the differential equation by using conical boundaries. Following this approach, Browne, Friedman, and Hodes in reference 2 obtained a solution for the pressure field of a wing-body combination composed of a flat triangular wing and a cone both with a common apex. The use of all-conical boundaries reduces the problem to one of conical flow for which powerful methods of solution are available.

Several investigators have presented methods for determining the pressure field, including the effect of interference, acting on wing-body combinations employing circular fuselages and wings not necessarily slender. In reference 3, Ferrari has given an approximate method of obtaining the "interference of the wing on the streamlined body, assuming that the induced field generated by the wing is that which would exist around the wing if it were placed in the uniform stream alone." Similarly, the interference of the body on the wing has been determined. The results of Ferrari thus represent a first approximation and, while a second approximation using the method is possible in principle, it appears that too much labor would be involved.

Another method for estimating the effect of interference on the aerodynamic properties of wing-body combinations which are not necessarily slender is given in reference 4. In this reference the method is applied to determining the drag of symmetrical wing-body combinations; it is also applicable to the calculations of the lifting pressures acting on combinations employing wings with supersonic edges. In reference 5, an essentially new method of solving a wide class of wing-body interference problems has been presented. The method is based on decomposing the interference of a wing-body combination into a number of Fourier components and solving the problem for each component in a manner similar to that used by von Kármán and Moore in reference 6 for bodies of revolution.

To summarize the present situation, it can be said that the existing interference methods fall into two categories. The first category includes those attempts to solve difficult boundary-value problems as in references 3, 4, 5, and 7. These methods have the shortcomings that they all involve a great deal of labor, and that, with the exception of reference 5, they represent approximations to the true linear-theory solutions. The second category includes simpler methods such as those of references 1, 2, and 8 and existing approximate engineering methods. These methods have the disadvantages of being applicable only to specialized configurations or of being based on assumptions of unknown validity.

At the present time, there is a definite need for a simplified general theory of wing-body interference that will give results of engineering accuracy for a wide range of wing aspect ratio, taper ratio, leading-edge sweepback angle, and span-diameter ratio. The reasons that none has yet been developed are twofold: first, the lack of systematic experimental results makes an empirical theory difficult; and second, incomplete knowledge of the mechanism of wing-body interference, because of the shortage of exact solutions, makes it difficult to develop a reliable rational method. The development of a simple general theory of wing-body interference seems thus to be dependent on obtaining a few exact solutions that will give sufficient insight into the mechanism of interference to permit valid simplifying assumptions. Such solutions are also necessary to assess the validity of the assumptions underlying present theories.

In reference 5, a solution has been obtained to a wing-body problem that is exact within the limitations of linear theory. It is the purpose of this paper to present a résumé of reference 5 with special emphasis on the physical principles underlying the interference. It is hoped that the insight gained into the mechanism of interference in this paper will be sufficient to allow the development of a simple, reliable engineering method.

In this paper, a physical description of the interference problem will be given, and an illustrative example of a rectangular wing at incidence on a round body at zero angle of attack will be presented in detail.

SYMBOLS

a	body radius
A	aspect ratio of wing formed by joining exposed half-wings together
c	chord of rectangular wing
c^*	effective chord-radius ratio $\left(\frac{c}{\beta a}\right)$
C_D	minimum wave drag coefficient of wing based on exposed wing area
c_r	chord at wing-body juncture
c_t	chord at wing tip

$f_{2n}(x)$	velocity amplitude function of n'th Fourier component
$g_{2n}(x)$	axial strength function of n'th Fourier component
$h_{2n}(x)$	axial strength function for unit step in $f_{2n}(x)$ at origin
k_W	$\frac{L_{WC}}{L_W}$
$K_{2n}(\tau,r)$	function used in determining P_{2n}
L_W	lift on exposed half-wings joined together
L_{WC}	lift on exposed half-wings in combination with body
L	lift
L_{2n}	lift due to n'th Fourier component
m	odd integer
M	free-stream Mach number
$M_{2n}(x),W_{2n}(x)$	characteristic functions
n	number of Fourier component
P	pressure coefficient $\left(-\frac{2u}{V}\right)$
P_{2n}	interference pressure coefficient due to n'th Fourier component
q	free-stream dynamic pressure
r,θ,x	cylindrical coordinates: $y = r \cos \theta$, $z = r \sin \theta$ (See fig. 1.)
s	semispan of wing-body combination
t	maximum wing thickness
$\left(\frac{t}{c}\right)$	thickness ratio of double-wedge wing
u,v,w	axial, lateral, and vertical perturbation velocities, respectively

x,y,z	Cartesian coordinates: x, axial coordinate; y, lateral coordinate; z, vertical coordinate (See fig. 1.)
$x_{c.p.}$	center of pressure of wing lift measured from wing leading edge
V	free-stream velocity
α_B	body angle of attack
α_l	local angle of attack $\left(-\frac{w}{V}\right)$
α_u	upwash angle of body-alone flow
α_W	wing angle of attack
β	$\sqrt{M^2-1}$
βA	effective aspect ratio
δ	$\sin^{-1}x$
λ	taper $\left(\frac{c_t}{c_r}\right)$
ξ,τ	dummy variables of integration
Λ	sweep angle of wing leading edge
φ	interference perturbation velocity potential
φ_C	combination perturbation velocity potential
φ_W	wing-alone perturbation velocity potential
φ_{2n}	n'th Fourier component perturbation velocity potential
$\varphi_{2n}*(r,\theta,x)$	fundamental solution for n'th Fourier component
$\psi(x,r)$	undetermined function of x and r

PHYSICAL PRINCIPLES

Prior to a mathematical formulation of the wing-body interference problem, it is well to define interference and to explain how it arises. With a stationary wing or a stationary body in a uniform parallel flow, there are associated the wing-alone and body-alone flow fields. If the wing is immersed in the body-alone flow field, the fluid velocity due to the body-alone field will not, in general, be tangential to the wing (or conversely). For this reason, the sum of the body-alone plus wing-alone flow fields will not be the flow field for the body and wing together. The difference between the flow field of the body and wing together and the sum of the body-alone and wing-alone flow fields is defined to be the interference flow field.

Effect of Forebody on Wing

The effects of wing-body interference on the flow field of a wing-body combination are illustrated by considering separately the effects of each component on the others. For the purposes of this discussion figure 1 shows a wing-body combination divided into the part in front of the leading edge of the wing-body juncture, henceforth called the nose, the winged part and the part behind the wing trailing edge, henceforth called the afterbody. The wing may be twisted and cambered, but it is assumed to have supersonic leading edges. Consider now the flow as it progresses past the body. At the body nose the flow is that around a body of revolution, and it can be treated by existing methods such as those of references 1, 6, and 9. When the body is at angle of attack α_B, there is an upwash field in the horizontal plane of symmetry of the body. If the body is sufficiently slender, the flow field in a plane at right angles to the body axis corresponds to that around a circular cylinder in a uniform stream of velocity, $V \sin \alpha_B$. This gives an upwash field in the horizontal plane of symmetry of the body of

$$\alpha_u = \alpha_B \left(1 + a^2/y^2\right) \tag{1}$$

The effect of this upwash on the wing can be obtained by considering the wing to be at angle of attack and twisted according to equation (1) and by applying the formulas of supersonic wing theory. The wing pressure field so obtained is exact, within the limitations of the theory, for that section of the wing outboard of the Mach line emanating from the leading edge of the wing-body juncture. If the wing is located close to the body nose so that there is a chordwise variation in the upwash field due to the body, then the wing is effectively cambered, and the solution is more difficult. However, for most wing-body combinations it is possible to disregard the effect of the nose, and to assume that the wing is attached to a circular cylinder that extends upstream indefinitely.

Mutual Effects Between Body and Wing

The mutual interference between the body and wing on the winged part of a combination causes an interference field acting on the body and on the wing inboard of the Mach line emanating from the leading edge of the wing-body juncture.

The wing-alone flow field does not, in general, produce flow tangential to the position to be occupied by the body surface. An interference flow field must arise that cancels the velocity induced by the wing-alone flow field normal to the body while not changing the body shape. Alternately, the origin of the interference field can be explained in the following manner. The wing and body can be thought of as sources of pressure disturbances that radiate in all directions in downstream Mach cones. The wing disturbances which radiate toward the body are in part reflected back by the body onto the wing and in part transmitted onto the body giving rise to interference pressures. Likewise, the disturbances originating on the body pass onto the wing and affect the pressures there. It is apparent that the determination of the interference pressure field on the body and on the wing inboard of the Mach line of the juncture is the crux of the wing-body interference problem.

Mutual Effects Between Wing Panels

To determine the region of influence of one wing panel on another, it is necessary to trace the path of a pulse from one wing panel across the body onto the other. The path traced across the body by the pulse originating at the leading edge of the wing-body juncture is the forward boundary of the region of influence of one wing panel on the body. (See fig. 1.) It is clearly the helix intersecting all parallel elements of the cylinder at the Mach angle. The boundary crosses the top of the body a distance of $\frac{\pi a}{2}\sqrt{M^2-1}$ downstream and reaches the opposite wing-body juncture a distance $\pi a\sqrt{M^2-1}$ downstream. A pulse originating at a point on one wing panel and traveling to a point on the other panel can travel around the body on its surface to the opposite juncture and then along the wing to a given point, or it can leave the body tangentially before reaching the opposite wing juncture in a straight path to the point. The second means of transmitting the impulse is shorter in distance than the first and is the one which determines the forward boundary of the region of influence of one wing panel on the other. Applying this consideration to the pulse originating at the leading edge of one wing-body juncture, it is easy to show that the forward boundary of the region of influence of one wing panel on the opposite wing panel is given by the equation

$$\frac{x}{\sqrt{M^2-1}} = \left(\pi - \cos^{-1}\frac{a}{y}\right) a + \sqrt{y^2-a^2} \tag{2}$$

This boundary is also shown in figure 1, and it becomes parallel to the Mach direction at distances far from the body.

Effects on the Afterbody

As far as the interference effect of the body on the wing is concerned, it is confined to the winged part of the combination, but the effect of the wing on the body is felt also on the afterbody. If the downwash were known everywhere in the wing wake, then the wake could be considered as an extension of the wing with twist and camber. The wing wake and afterbody could then be incorporated with the winged part of the combination and treated in the same manner. However, the actual downwash pattern in the wing wake depends on the interference effect of the body on the wing. It is thus apparent that the solution of the afterbody problem requires that the interference problem for the winged part of the combination be solved first. Only the winged part of the combination is analyzed in detail in this report.

MATHEMATICAL FORMULATION OF THE PROBLEM

Throughout the analysis, the body radius is taken as unity and M^2 is taken as 2 so that $\beta = 1$. Any formula can be generalized to any body radius by dividing all length symbols by a, and to any Mach number by dividing all streamwise lengths by β, by multiplying all pressure and lift coefficients by β, and leaving all potentials, lift forces, and span loading unaltered. It is necessary to specify the wing alone before any detailed interference calculation can be carried out. However, in the theoretical solution of the problem the wing-alone definition is arbitrary. The flow field about the combination does not depend on the definition of the wing alone.

The analysis is confined to the cases for which the aspect ratios are sufficiently large that the Mach lines from the leading edges of the wing tips do not intersect the wing-body juncture. This is the case if the aspect ratio obeys the following inequality:

$$\beta A \geq \frac{4}{\left(1 + \lambda\right)\left(\frac{\tan\Lambda}{\beta} + 1\right)}$$

Under such circumstances, the tips have no influence on the wing-body interference of the winged part of the combination.

The wing-body combinations being considered in this report are those possessing a vertical plane of symmetry. To eliminate any questions of the symmetry of the boundary conditions above and below the wing, the assumption is made that the wings have supersonic leading and trailing edges. This assumption, together with that concerning tip effects, is sufficient to insure the fact that pressure communication between the upper and lower wing surfaces can have no effect on the interference on the winged part of the combination. Thus it is immaterial whether the problem at hand is symmetrical or antisymmetrical with regard to the horizontal plane of symmetry. Attention will henceforth be focused above the horizontal plane of symmetry.

The assumptions with regard to tip effects and the sweep of leading and trailing edges enable the drag of a symmetrical wing-body combination at zero angle of attack to be obtained from solutions for lifting surfaces. Suppose the problem solved is that for a flat wing at angle of attack α_W mounted on a body at zero angle of attack. The pressures are antisymmetric with respect to the horizontal plane of symmetry. However, considering the same pressures as positive and symmetrical yields the solution for the pressure field of a single-wedge wing of half angle α_W at zero angle of attack. This fact is of use in obtaining the drag coefficient at zero angle of attack, as will be illustrated.

General Decomposition of Boundary-Value Problem

The general case of the wing and body at different angles of attack is considered. Following the suggestion of Lagerstrom and Van Dyke in reference 10, the problem can be broken down into several simpler problems on the assumption that the wing boundary conditions can be applied in the plane of the wing and those for the body can be applied on a cylindrical surface. Figure 2 shows the decomposition of the wing-body combination into three components. Component (a) is simply the body alone, which creates an upwash field α_u in the region that is to be occupied by the wing. Components (b) and (c) are combinations with wings of the same plan form; but while component (b) has the wing-alone angle of attack, component (c) has a wing with angle of attack $-\alpha_u$. The significance of this particular method of decomposing the general wing-body problem is that component (a), the body alone, can be solved by known methods and components (b) and (c) with bodies at zero angle of attack can be solved by the methods of this report. Henceforth the analysis is confined to combinations with bodies at zero angle of attack.

Wing alone and interference potentials.- Consider now a combination with the body at zero angle of attack and let φ_C be its potential. (See fig. 3.) This potential can be considered the sum of a wing-alone potential φ_W and of an interference potential φ.

$$\varphi_C = \varphi_W + \varphi \tag{3}$$

The essential problem is to determine φ. First, select a convenient way of extending the wing through the body to form the wing alone, thereby specifying φ_W. The wing-alone flow field in general produces velocities $\frac{\partial \varphi_W}{\partial r}$ normal to the surface that will enclose the circular cylinder as illustrated in figure 3 for the region above the wing. In figure 3 and the subsequent figure, all bodies are shown as cylinders parallel to the x axis. While the bodies of the actual configurations in some cases are slightly distorted cylinders, they are nevertheless shown as true cylinders. This procedure is compatible with the fact that the boundary conditions are to be applied on a true cylinder. The value of $\frac{\partial\varphi_W}{\partial r}$ varies with θ and with x. This means that a body conforming to the wing-alone flow field is distorted in a complicated fashion. Now since the body must be circular, there must arise an interference potential φ that identically cancels $\frac{\partial\varphi_W}{\partial r}$ at the body surface, thereby straightening it.

$$\frac{\partial\varphi}{\partial r} = -\frac{\partial\varphi_W}{\partial r} \quad \text{at} \quad r = 1 \tag{4}$$

There are two other conditions to be fulfilled by φ. It must not distort the shape of the wing when added to φ_W to produce φ_C. Thus when $\theta = 0$,

$$\frac{\partial\varphi}{\partial\theta} = 0 \tag{5}$$

or $\alpha_W = 0$ for the interference combinations as shown in figure 3. The last condition is that the interference potential must be zero ahead of the winged part of the combination.

$$\varphi = 0 \; x \leq 0 \tag{6}$$

Equations (4), (5), and (6) are the essential boundary conditions on φ.

The normal velocity $\frac{\partial\varphi}{\partial r}$ to be induced at the body surface by the interference potential can be analyzed at any given streamwise position as a Fourier cosine series. The amplitudes of the various Fourier cosine terms, $f_{2n}(x)$, vary with x, the streamwise distance. Thus,

$$\frac{\partial\varphi}{\partial r} = \sum_{n=0}^{\infty} f_{2n}(x) \cos 2n\theta = -\frac{\partial\varphi_W}{\partial r} \quad \text{at} \quad r = 1 \tag{7}$$

Only even multiples of θ are considered because of the vertical plane of symmetry. Consider that the interference potential is decomposed into a series of potentials such that each cancels one Fourier component of the velocity at the body surface, that is,

$$\varphi = \sum_{n=0}^{\infty} \varphi_{2n} \tag{8}$$

with

$$\frac{\partial\varphi_{2n}}{\partial r} = f_{2n}(x) \cos 2n\theta \quad \text{at} \quad r = 1 \tag{9}$$

Then the combination giving the interference potential φ can be decomposed in a series of combinations each giving one of the φ_{2n} values. The decomposition is illustrated in figure 4. For $n = 0$,

$$\frac{\partial\varphi_0}{\partial r} = f_0(x)$$

and there is no variation of the normal velocity, pressure, or potential with θ. Thus the first interference combination is a body of revolution. The pressure field acting on the body of such a combination can be determined by the method of reference 11. This $n = 0$ interference combination has the very simple significance that its flow normal to the $r = 1$ cylinder, $\frac{\partial\varphi_0}{\partial r}$, subtracted from $\frac{\partial\varphi}{\partial r}$ reduces the flow across the body to zero when averaged from $\theta = 0$ to $\theta = \pi$ at any streamwise location. For $n = 1$,

$$\frac{\partial\varphi_2}{\partial r} = f_2(x) \cos 2\theta$$

and the normal velocity, pressure, and potential will vary as $\cos 2\theta$.

To summarize briefly, it has been shown that the general interference problem of a body and wing at different angles of attack can be broken down into wing-body problems with bodies at zero angle of attack as shown in figure 2. Combinations with the body at zero angle of attack are decomposed into wings alone plus interference combinations as in figure 3. The interference combinations are finally decomposed into their Fourier components as in figure 4.

A general method for determining the characteristics of any Fourier component will now be given. It will be shown that good accuracy can be obtained for the interference potential with few Fourier components.

Method of Solution

The problem to be solved is that of a supersonic wing-body combination subject to the conditions already mentioned, but with the wing and body possibly at different angles of attack. This problem is reduced to a body-alone problem and two wing-body problems with the body at zero angle of attack as shown in figure 2. The body-alone problem can be solved by existing methods such as references 6 and 9. The procedure necessary to solve either wing-body problem as given in reference 5 is now summarized.

Wing-alone potential and velocity amplitudes.- The first step in the solution is to determine the wing-alone potential, φ_W. The methods of wing theory available for doing this will not be discussed here. From the value of φ_W the value of the normal velocity induced at the $r = 1$ cylinder follows readily. This normal velocity distribution is expanded in a Fourier cosine series of even multiples of θ.

$$\frac{\partial\varphi_W}{\partial r} = -\sum_{n=0}^{\infty} f_{2n}(x) \cos 2n\theta \quad \text{at} \quad r = 1 \tag{10}$$

The functions $f_{2n}(x)$ are called the velocity amplitude functions and are part of the boundary conditions for the interference potential.

Interference potential.- The solution for the interference potential is obtained by summing the potentials for the series of Fourier component potentials. The determination of the potential for any one Fourier component (as illustrated by fig. 4) has been carried out formally in reference 5 by Laplace transform theory. It was shown that the formal mathematical solution is equivalent to distributing fundamental solutions for φ along the axis of the combination in a manner similar to that of von Kármán and Moore in reference 6. Let $\varphi_{2n}^*(x-\xi,r,\theta)$ be the fundamental solution located at $x = \xi$ to be used in determining the potential of the n'th Fourier interference component. Let $g_{2n}^*(\xi)$ be the distribution of this solution along the body axis from $x = -1$ to $x = \infty$ to satisfy the boundary conditions. Then the potential of the n'th Fourier component is

$$\varphi_{2n}(x,r,\theta) = \int_{-1}^{x-r} \varphi_{2n}^*(x-\xi,r,\theta)\, g_{2n}^*(\xi)\, d\xi$$

First, the set of fundamental solutions $\varphi_{2n}^*(x,r,\theta)$ will be presented, and then the method of obtaining $g_{2n}^*(\xi)$ will be discussed.

Axial strength function.- The boundary conditions to be satisfied by each Fourier component of the interference potential are given by equations (5), (6), and (9). The first two boundary conditions are satisfied by choosing an appropriate set of fundamental solutions. Such a set of fundamental solutions, derived in appendix A, is

$$\varphi_{2n}^*(x-\xi,r,\theta) = \frac{\cos 2n\theta}{r^{2n}} \frac{\partial^{2n-1}}{\partial x^{2n-1}} \left[(x-\xi)^2-r^2\right]^{2n-\frac{1}{2}} \tag{11}$$

The fundamental solution is located at the point $x = \xi$, and the value of ξ varies from -1 to $+\infty$. For $n = 0$ an integration is to be performed. The last boundary condition is satisfied by distributing fundamental solutions, as given in equation (11), along the body axis in variable strength. In appendix B the following equation is derived for determining the axial strength function

$$g_{2n}(x) = 2^{2n} \frac{(2n!)}{(4n!)} \int_{0}^{x} M_{2n}(x-\xi)\, f_{2n}'(\xi)\, d\xi \tag{12}$$

The evaluation of $g_{2n}(x)$ from this equation is done numerically or graphically. The values of $f_{2n}'(x)$ are obtained on the basis of equation (10). A table of the functions $M_{2n}(x)$ are included as table I for use in equation (12), and figure 5 illustrates these functions. The properties of $M_{2n}(x)$ are discussed in reference 5.

Potential or span loading.- Once the axial strength distribution of the fundamental solution is known, the determination of the interference potential or pressure follows readily. Consider the general point P, shown in figure 6, where the potential is to be determined. The fundamental solution along the axis from -1 to x-r influences the potential at P which is given as

$$\varphi_{2n}(x,r,\theta) = \int_{-1}^{x-r} \frac{\cos 2n\theta}{r^{2n}} \frac{\partial^{2n-1}}{\partial x^{2n-1}} \left[(x-\xi)^2-r^2\right]^{2n-\frac{1}{2}} g_{2n}*(\xi)\, d\xi \tag{13}$$

By making a unit translation of the variable of integration so that the lower limit is zero, there is easily obtained

$$\varphi_{2n}(x,r,\theta) = \frac{\cos 2n\theta}{r^{2n}} \int_{0}^{x-r+1} \frac{\partial^{2n-1}}{\partial x^{2n-1}}$$

$$\left[(x-\xi+1)^2-r^2\right]^{2n-\frac{1}{2}} g_{2n}(\xi)\, d\xi \tag{14}$$

Equation (14) serves to determine the potential anywhere in the flow field once the axial strength function $g_{2n}(x)$ has been obtained. Since the integrated lift per unit span up to a given streamwise position x is proportional to φ at that position, equation (14) also gives the span loading.

Pressure coefficient.- On the basis of linear theory, the pressure coefficient is

$$P = -\frac{2u}{V} = -2\,\frac{\partial\varphi/\partial x}{V} \tag{15}$$

With the aid of equation (15) it is readily shown from equation (14) that

$$P_{2n} = -2\,\frac{\cos 2n\theta}{V}\int_0^{x-r+1} K_{2n}(\tau,r)\; g_{2n}(x-r+1-\tau)\; d\tau \tag{16}$$

where

$$K_{2n}(\tau,r) = \frac{1}{r^{2n}}\,\frac{\partial^{2n}[\tau(\tau+2r)]^{2n-\frac{1}{2}}}{\partial\tau^{2n}}$$

The procedure in obtaining the pressure coefficient is first to obtain the axial strength function from equation (12) by numerical or graphical integration, and then to obtain P_{2n} for any point in the flow field from equation (16) by the same means.

Body pressure coefficient.- The determination of the pressure coefficient by the method outlined requires two numerical or graphical integrations. In appendix C a simpler method involving only one integration is derived for the body pressure coefficient. The result for the pressure coefficient is

$$P_{2n} = \frac{2}{V}\cos 2n\theta\; f_{2n}(x) - \frac{2}{V}\cos 2n\theta\int_0^{x} f_{2n}(\xi)W_{2n}(x-\xi)\; d\xi \tag{17}$$

at $r = 1$. The functions $W_{2n}(x)$ are universal functions. They are tabulated in table II, and are plotted in figure 7.

Combination potential.- The combination potential is obtained by simply adding the wing-alone potential to the interference potential φ. The interference potential φ is obtained as already described by adding together the interference potentials of a number of Fourier component combinations. The lift or pressure coefficients for the combination are similarly obtained simply by adding to those for the wing alone those for the interference combination.

Referring again to figure 2, the detailed method for solving either cases (b) or (c) has been summarized. To solve the general case of both body and wing at angle of attack, both (b) and (c) must be solved. The wing alone for each case is different. The simplest interference problem is that for the body at zero angle of attack. Under these circumstances, α_u is zero, and only case (b) must be solved. This case will be calculated for a rectangular wing-body combination as an illustrative example.

PRESSURE FIELD ACTING ON A COMBINATION WITH RECTANGULAR WINGS

One of the simplest wing-body combinations of technological importance is that formed by a rectangular wing mounted at incidence on a circular body at zero angle of attack. The complete pressure field acting on such a combination will now be determined. The results are interpreted in terms of lift and center of pressure presented as a function of effective aspect ratio and effective chord-radius ratio. As previously mentioned, the wing alone can be specified in any convenient manner and, for the purpose of the example, the wing alone is taken as the rectangular wing extending straight through the body from side to side. Although the analysis as carried out is for $M = \sqrt{2}$, the results are presented in a form applicable to a range of Mach numbers. The steps in performing the calculation are: (1) to determine φ_W, the wing-alone potential; (2) to determine the velocity amplitude functions, $f_{2n}(x)$; (3) to determine the axial strength functions, $g_{2n}(x)$; and (4) to determine the potential or pressure, as desired, anywhere in the field. No tip effects are considered until the results are presented as a function of wing aspect ratio.

Wing-Alone Potential

The wing-alone flow, exclusive of tip effects, can be determined from the Ackeret theory. The flow at a spanwise station out of the region of influence of the wing tips is illustrated in figure 8. The potential for the flow above the wing is

$$\varphi_W = Vx \quad \text{when} \quad z \geq x \tag{18}$$

$$\varphi_W = Vx + \alpha_W V(x-z) \quad \text{when} \quad z \leq x \tag{19}$$

The sidewash produced by such a potential $\frac{\partial\varphi_W}{\partial y}$ is zero and the downwash $\frac{\partial\varphi_W}{\partial z}$ is uniformly $-\alpha_W V$. The downwash causes a flow normal to the surface $r = 1$ in amount $-\alpha_W V \sin\theta$. This means that for a body conforming to the wing-alone flow, the deformation is zero at the wing-body junctures and a maximum on the top of the body. The interference combinations when added to the deformed body straighten it out Fourier component by Fourier component.

Fourier Amplitudes of Body Normal Velocity

The Fourier amplitudes of the normal velocity induced by the wing-alone potential at the body is determined by expanding $\frac{\partial\varphi_W}{\partial r}$ at $r = 1$

in a Fourier cosine series of even multiples of θ. The normal velocity distribution is shown in figure 9. For $x \geq 1$ the body is totally immersed in the wing downwash field. With the usual equation for obtaining the Fourier amplitudes of a function, there is obtained

$$f_o(x) = \frac{2}{\pi}\int_0^{\sin^{-1}x} \alpha_W V \sin\theta \, d\theta \tag{20}$$

$$f_{2n}(x) = \frac{4}{\pi}\int_0^{\sin^{-1}x} \alpha_W V \sin\theta \cos 2n\theta \, d\theta \tag{21}$$

The integrations give

$$f_o(x) = \frac{2V\alpha_W}{\pi}\left(1 - \sqrt{1-x^2}\right) \quad \text{when} \quad x \leq 1 \tag{22}$$

$$f_o(x) = \frac{2V\alpha_W}{\pi} \quad \text{when} \quad x \geq 1 \tag{23}$$

$$f_{2n}(x) = \frac{V\alpha_W}{\pi}\left[\frac{2\cos(2n-1)\delta}{2n-1} - \frac{2\cos(2n+1)\delta}{2n+1} - \frac{4}{4n^2-1}\right] \quad \text{when} \quad x \leq 1 \tag{24}$$

$$f_{2n}(x) = \frac{-4V\alpha_W}{\pi(4n^2-1)} \quad \text{when} \quad x \geq 1 \tag{25}$$

where $\delta = \sin^{-1}x$. The $f_{2n}(x)$ functions are shown in figure 10. The constant values of $f_{2n}(x)$ for $x \geq 1$ are noteworthy.

Axial Strength Functions

The calculation of the axial strength distributions has been carried out with the aid of equation (12). The integrations were performed numerically by means of integration formulas given in reference 12. Two separate cases occur, $x < 1$ and $x > 1$. For $x < 1$ a typical plot of the integrand and its components is shown in figure 11(a). It will be observed that the $M_o(x-\xi)$ function has a singularity at the upper limit of integration. Since the singularity is of the square root type, it is easily handled. For $x > 1$ the determination of $g_o(x)$ is complicated by the fact that $f_o'(\xi)$ has a square root singularity at $\xi = 1$, but simplified by the fact that $f_o'(\xi)$ is zero for $\xi > 1$. A typical plot of the integrand and its components for $x > 1$ is shown in figure 11(b). The singularity of $M_o(x-\xi)$ has been replaced by that of $f_o'(\xi)$ at the upper limit of integration. For $x = 1$ the square root singularities of $M_o(x-\xi)$ and $f_o'(\xi)$ both occur at $\xi = 1$, reinforcing each other in such a manner that $g_o(x)$ has a logarithmic singularity at $x = 1$. In fact, it can be shown that

$$g_{2n}(x) \rightarrow \frac{2^{2n}(2n!)}{(4n!)} (-1)^n \left(\frac{4}{\pi}\right) \frac{V\alpha_W}{\pi} \log|1-x|$$

in the neighborhood of $x = 1$. The function $g_{2n}(x)$ minus the logarithmic term passes smoothly through $x = 1$.

A plot of the $g_{2n}(x)$ functions for $n = 0$ to $n = 3$ is shown in figure 12. The main effect noted is that the number of times the curve crosses the zero axis increases as the order of the $g_{2n}(x)$ functions increases. The singularities at $x = 1$ are also illustrated.

Pressure Distributions

Obtaining the strength functions of $g_{2n}(x)$ is tantamount to getting the potential or pressure coefficient anywhere in the flow field as given by equation (14) or (16). If only the span load distribution is required, then one calculation using equation (14) suffices for each spanwise station; but if the detailed pressure distribution is required, then many calculations using equation (16) must be made for each station. The detailed pressure distributions have been calculated using equations (16) and (17). In equation (16), the factor

$$K_{2n}(\tau,r) = \frac{1}{r^{2n}} \frac{\partial^{2n}}{\partial\tau^{2n}} [\tau(\tau+2r)]^{2n-\frac{1}{2}}$$

appears inside the integral as an influence coefficient for converting axial strength function into pressure coefficient. The factor plays an important role in determining the accuracy of the numerical work. In figure 13 plots of $K_o(\tau,r)$ and $K_2(\tau,r)$ are presented showing the singularities of $K_{2n}(\tau,r)$ at the origin of τ. These singularities, together with those of $g_{2n}(x-r+1-\tau)$ at $\tau = x-r$, bring about two different cases in the determination of the pressure coefficient. If $x<r$, only the $K_{2n}(\tau,r)$ singularity occurs in the integration as illustrated by figure 14(a). However, for $x>r$ there are two singularities as shown in figure 14(b). For $x = r$ the two singularities come into confluence, but they still produce a finite pressure coefficient.

Interference pressure distribution.- The interference pressure distributions have been calculated for the first four Fourier components and are presented in figure 15. In this figure the abscissa is proportional to distance behind the Mach line originating at the leading edge of the juncture, as illustrated in the figure. Although the calculations have been carried out for $M = \sqrt{2}$, that is, $\beta = 1$, and for unit radius, they are generalized to all Mach numbers and body radii by replacing $x-r+1$ by $\frac{x}{\beta a} - \frac{r}{a} + 1$ and P_{2n} by βP_{2n} as has been done in the figure. From the figure it is apparent that the cusps in the pressure distributions are propagated downstream along lines of constant $\frac{x}{\beta a} - \frac{r}{a} + 1$ or $x-\beta r$; that is, along the downstream characteristics. As the pressure distributions move outward from the body along the downstream characteristics, they are distorted and decreased in magnitude.

Increasing the order of the Fourier harmonics causes two important effects: first, the number of points of zero pressure is increased and, second, the pressure coefficient damps more rapidly. As a result of the first effect the contributions of the higher harmonics to the combination span loading are proportionally less than their contributions to the pressure coefficient; while as a result of the second effect the more remote a point is from the leading edge of the wing-body juncture, the fewer the number of Fourier components that must be included to obtain its pressure coefficient accurately. All interference pressure distributions exhibit discontinuities in slope at $\frac{x}{\beta a} - \frac{r}{a} + 1 = 1$. This behavior is a consequence of the fact that the body becomes totally immersed in the wing-alone flow field for this condition. When the pressure distributions of the various Fourier components are added together to obtain the interference pressure distributions, the discontinuities in slope tend to cancel so that the pressure distribution for the combination will be smooth.

A detailed examination of the interference pressure distribution for the first Fourier component illustrates several points of interest. The importance of the component arises from the fact that it accounts for most of the effect of interference on the span loading. The reason for this is that the pressure coefficients for $n = 0$ are of invariable sign. The effect of the first Fourier component is to reduce the velocity induced normal to the body by the wing-alone flow field to zero average around the body for $\theta = 0$ to $\theta = \pi$ at any streamwise location.

For purposes of comparison with the exact results for $n = 0$, some approximate results have been included in figure 15(a). For values of $\frac{x}{\beta a} < 1$ on the body, the Ackeret value of P_0 (twice the local stream angle divided by β) is a close approximation to the true pressure coefficient. This is the result of the facts that the part of the body affecting the interference is effectively plane for points near the leading edge of the wing-body juncture and that there is no variation of any quantities with θ so that an approximate two-dimensional situation prevails. As $\frac{x}{\beta a}$ increases beyond unity on the body, there is a rapid decrease in the pressure coefficient below the Ackeret value due to the effect of all disturbances in front of the point in question as represented by the integral of equation (17).

In reference 5, the following approximate results were obtained for small and large values of $\left(\frac{x}{\beta a} - \frac{r}{a} + 1\right)$ for the pressure coefficient:

$$\beta P_{2n} \rightarrow \frac{4\alpha_W \cos 2n\theta}{\pi\sqrt{r}} \left(\frac{x}{\beta a} - \frac{r}{a} + 1\right)^2; \quad \frac{x}{\beta a} - \frac{r}{a} + 1 \rightarrow 0 \tag{26}$$

$$\beta P_0 \rightarrow \frac{4\alpha_W}{\pi x/\beta a}; \quad \frac{x}{\beta a} - \frac{r}{a} + 1 \rightarrow \infty \tag{27}$$

Figure 15(a) shows that for values of $\frac{x}{\beta a} - \frac{r}{a} + 1 \leq 0.6$ equation (26) is a good approximation for $n = 0$ although it is of little value for higher-order harmonics. There is a general tendency of P_0 to approach a uniform value independent of r as $\frac{x}{\beta a} - \frac{r}{a} + 1$ becomes large, as shown by equation (27). The damping in the characteristic direction, although initially inversely proportional to the square root of r, is ultimately independent of r.

The pressure distributions of figure 15 were determined by equation (17) for $r = 1$, and by equations (12) and (16) for $r = 1.5$, 2.0, and 3.0. However, the values for $r = 1$ were checked by equations (12) and (16) before these equations were applied to the higher values of r. For $r = 1$ equation (17) gives more accurate results than equations (12) and (16) since it requires only one numerical integration. The accuracy of both methods of calculation decreases as n and $\frac{x}{\beta a} - \frac{r}{a} + 1$ increase because the small values of the pressure coefficients under these conditions are the result of large counterbalancing influences.

Pressure distribution in juncture of wing-body combination.- By adding the interference pressure coefficients of the various Fourier components to that for the wing alone, the pressure distribution for the combination is obtained. The addition has been carried out for the wing-body juncture using four Fourier components and six Fourier components, and the results are presented in figure 16. The pressure coefficient with interference is less in magnitude than two, the value without interference, showing that significant losses of lift occur in the wing-body juncture. A comparison of the results for four components and six components shows that four components give good over-all accuracy for all values of $\frac{x}{\beta a}$ greater than 1. For small values of $\frac{x}{\beta a}$ in the wing-body juncture, the curvature of the body insofar as the flow is concerned is not large so that the body is effectively a vertical boundary on which a given distribution of normal velocity is producing an interference field. Supersonic wing theory applied to this condition gives for the net interference pressure coefficient (reference 5)

$$\frac{\beta P}{\alpha_W} \rightarrow \frac{4x}{3\pi\beta a} \text{ when } \frac{x}{\beta a} \rightarrow 0 \qquad (28)$$

It is clear that the calculated results can be joined smoothly to this result. Using the result of equation (28) enables satisfactory results to be obtained with four Fourier components.

The critical region in the convergence of the solution is that near the leading edge of the wing-body juncture. The higher harmonics have their most important effect near here, and rapidly damp downstream along the body. Hence more and more Fourier components would be required to get accuracy for smaller and smaller values of $\frac{x}{\beta a}$. However, with the result of equation (28), this extra work is unnecessary.

One point of interest in figure 16 is the fact that when $\frac{x}{\beta a}$ equals approximately 3, the pressure coefficient increases in magnitude. This is due to the fact that for $\frac{x}{\beta a} \geq \pi$ the influence of the opposite half-wing is felt in the wing-body juncture.

Pressure distribution on top meridian of wing-body combination.- The pressure distribution on the top meridian of the wing-body combination is obtained in the same fashion as that at the wing-body juncture, the difference being that the pressures due to the even number Fourier components have the same sign at the meridian as at the juncture, whereas the odd numbered components have reversed signs. The pressure distributions based on four and six Fourier components are shown in figure 17.

Several interesting effects are exhibited by the results. The step in the wing-alone pressure at $\frac{x}{\beta a} = 1$ is effectively canceled by the interference pressures of the Fourier components from $\frac{x}{\beta a} = 1$ to $\frac{x}{\beta a} = \pi/2$, and for $\frac{x}{\beta a} > \pi/2$ the pressure increases rapidly and tends toward the two-dimensional value. The effect of the interference pressure in canceling the effect of the wing alone on the top of the body from $\frac{x}{\beta a} = 1$ to $\frac{x}{\beta a} = \pi/2$ is to be expected since the wing of the combination can have no effect on the top of the body unless $\frac{x}{\beta a} \geq \pi/2$, as has been already pointed out. If an infinite number of Fourier components had been taken, the pressure coefficients would be identically zero from $\frac{x}{\beta a} = 0$ to $\frac{x}{\beta a} = \pi/2$. The general behavior in this regard is evidence of the plausibility of the calculated results.

The tendency of the pressures to approach an asymptotic value is also illustrated by figure 17. This asymptotic value represented by the sum of the wing-alone pressure plus the asymptotic results for the first Fourier component is given by the following equation:

$$\frac{\beta P}{\alpha_W} \approx -2 + \frac{4}{\pi x/\beta a} \quad \text{when} \quad \frac{x}{\beta a} > 2.4 \tag{29}$$

For $\frac{x}{\beta a} > 2.4$, the results of this equation are in good agreement with the results of figure 17.

Some evidence is furnished from the pressure calculations for the juncture and top of the body concerning the number of Fourier components necessary for accuracy. Comparisons made in figures 16 and 17 show that about four components are sufficient, and that the addition of two more is not worth the extra work.

Pressure distributions for wing of wing-body combination.- The distribution of the pressure acting on the wing of the combination can be determined in a manner similar to that for the wing-body juncture by adding to the wing-alone pressure those due to the Fourier components. The resultant pressure distribution for the wing based on four Fourier components is shown in figure 18. A drawing of the pressure field for the complete configuration is included as figure 19. For small values of $\frac{x}{\beta a}$ the higher-order oscillations in the pressure coefficient as shown in figure 16 have been ignored and the curves have been faired through them.

Since the region of influence of the body on the wing is confined to the wing region downstream of the Mach lines emanating from the leading edge of the juncture, in front of this line the pressures are uniform at the two-dimensional value and behind the line there is a decrease in the magnitude of the pressure coefficient. If the body were a perfect reflector, that is, a vertical wall of infinite extent, then there would be no pressure loss. However, the pressure pulses originating on the wing are only in part reflected by the circular body. The efficiency of the body as a reflector is discussed subsequently in connection with span loading. The tendency of the pressure to increase in magnitude near the inboard trailing edge is due to the effect of the opposite wing panel which at the wing juncture is felt downstream of the point $\frac{x}{\beta a} = \pi$.

Span Loading

The span load distributions for a range of rectangular wing-body combinations with the body at zero angle of attack can be determined from the pressure distributions of figure 18. For purposes of specifying the span loading the following equation is used:

$$\left.\begin{aligned}\frac{L}{q\alpha_W} &= \int_{-s}^{+s}\left[-\int_{0}^{c/\beta}\frac{2\beta P}{\alpha_W}\,d\left(\frac{x}{\beta}\right)\right]dy \\ &= \int_{-s}^{+s}\left(-\int_{0}^{c}\frac{2P}{\alpha_W}\,dx\right)dy\end{aligned}\right\} \qquad (30)$$

The span loading is taken as the quantity inside the brackets.

The pressure results of figure 18 are for values of the effective chord-radius ratio of 4 or less and for values of the effective aspect ratio of 2 or greater. Span loadings for any combination of $\frac{c}{\beta a}$ (or c^*) and βA in these ranges can be obtained by integrating the pressure distributions. The span loading evaluations have been made for $c^* = 4$ and $\beta A \geq 2$. First the span loadings due to the various Fourier components are discussed, and then the span loadings for the actual wing-body combinations are presented.

Fourier component combinations.- In figure 20, the contributions to the span loading for the first three Fourier components are shown. For $n = 0$ the pressure field does not depend on θ, being axially symmetric, and a constant loading exists on the body. However, on the wing as the spanwise distance increases there is a decrease in the span loading due primarily to decrease in the length of chord over which the interference pressures act. The span loading due to the first Fourier component causes a loss of lift everywhere along the span.

A comparison of the results of figure 20 for $n = 0$ and $n = 1$ shows that the first Fourier component accounts almost entirely for the effect of interference on the span loading of the combination. For the body this fact is even more true than for the wing. This fact is of considerable importance since it gives a simple means of extending the lift and moment results to larger values of $\frac{c}{\beta a}$ than those for which the pressure distributions have been calculated. Also, it suggests a simple means of minimizing the adverse effects of interference on lift as will subsequently be pointed out.

With the techniques of Laplace transform theory, it is possible to obtain asymptotic formulas for the span loadings of the various Fourier components. For the first Fourier component the following asymptotic result has been obtained by the standard methods of Laplace transform theory. (See reference 5.)

$$-2\int_{0}^{x}\frac{P_0}{\alpha_W}\,dx \rightarrow \frac{8}{\pi}\log\left(\frac{r/2}{x/\beta a}\right) + \frac{2}{x/\beta a} \quad \text{when} \quad \frac{x}{\beta a} \rightarrow \infty \qquad (31)$$

The asymptotic result for the span loading given by this equation, when compared with the results of the exact calculations in figure 20, is seen to be slightly high. However, for values of $\frac{c}{\beta a}$ greater than 4 the difference between the results decreases, and equation (31) thus provides a satisfactory means of extrapolating the results of the present calculations for span loading to larger values of $\frac{c}{\beta a}$.

The asymptotic result has also been determined for the higher-order Fourier components as a matter of interest. The span loading is

$$-2\int_0^x \frac{P_{2n}}{\alpha_W}\,dx \rightarrow \frac{8\cos 2n\theta}{\pi n(4n^2-1)r^{2n}} - \frac{16\left(r^{2n}+\frac{1}{r^{2n}}\right)(4n-1)!\cos 2n\theta}{\pi(2n!)^2(4n^2-1)2^{4n-1}\left(\frac{x}{\beta a}\right)^{4n}} \quad \text{as} \quad \frac{x}{\beta a} \rightarrow \infty \tag{32}$$

A comparison between the results of equation (32) and the exact solution for $n = 1$ in figure 20 shows agreement and corroborates the fact that the span loading of all but the first Fourier component is negligible for $\frac{c}{\beta a} > 4$. It is also to be noted that the contribution to the loading of the first component given by equation (31) increases without limit as $x \rightarrow \infty$, whereas the span loading of the higher-order components is finite.

Family of complete combinations.- To obtain the span loading for the family of combinations for which $\frac{c}{\beta a} = 4$, it is necessary to consider the loading of both the wing alone and the Fourier components. The necessary calculations have been carried out and the span loadings for the family of combinations based on one and four Fourier components are both shown in figure 21. The loading due to the wing alone is also shown. No effect of wing tips has been included. It is to be noted in figure 21 that, whereas the loading on the wing due to its own pressure field is constant, there is some loss on the body because of the fact that the pressure field of the wing alone acts on the body only if $x \geq \beta a \sin\theta$. However, if an afterbody is included, some of the lift lost can be recovered. As has already been pointed out, the pressures due to the first Fourier components are positive on the upper half of the wing-body combination and produce a loss of lift, as figure 21 shows. When the effects of four Fourier components are taken into account, the net lift is slightly higher than that for one Fourier component, but the difference is not significant. For most engineering purposes, one Fourier component is sufficient for determining the span loading when $\frac{c}{\beta a} > 4$.

Some insight into the mechanism of wing-body interference can be gained by comparing the span loading for the combination with those for two reference loadings: (1) the complete reflection case for which the blanketed area of the wing acts effectively at α_W, and (2) the no-reflection case for which the blanketed area of the wing is supposed to act effectively at zero angle of attack. The span loading corresponding to the first case of complete reflection of the wing pressure pulses by the body is, in fact, the span loading marked "wing alone" in figure 21. A comparison of this curve with that based on one or four Fourier components shows that the loading given on the assumption that the wing blanketed area is fully effective in lift is too optimistic. Under the conditions of the second reference loading, the sole purpose of the blanketed area is to support lift generated by the wings. A comparison of the span loading for this case with the true loading shows that the average load on the body is well predicted, but that the loading on the wing is, of course, underestimated. A comparison of the true loading with those for the two reference cases reveals the interesting fact that the body is somewhat less than 50 percent effective in reflection for this particular family of configurations.

Lift

For values of $\frac{c}{\beta a}<4$ the pressure distributions already presented are sufficient for obtaining span loading or lift on either the wing or body for all combinations having sufficiently large aspect ratios to avoid effects of the tips on the wing-body interference. This is the case for $\beta A>2$. For values of $\frac{c}{\beta a}$ larger than four, the lift results are presented in terms of a nondimensional parameter k_W, defined as the ratio of the lift on the exposed half-wings in combination (exclusive of that on the body) to that on the exposed half-wings joined together.

$$k_W = \frac{L_{WC}}{L_W} \tag{33}$$

For $\frac{c}{\beta a}>4$ the value of k_W can be obtained by using the asymptotic form of the span loading given by equation (31).

$$k_W \sim 1-\frac{\left[\frac{2}{\pi c^*}-\frac{1}{2c^{*2}}-\frac{2}{\pi c^*}\log\left(\frac{\beta A}{4}+\frac{1}{2c^*}\right)-\frac{4}{\pi c^{*2}\beta A}\log\left(\frac{\beta A c^*}{2}+1\right)\right]}{\left(1-\frac{1}{2\beta A}\right)};$$

$$c^* \longrightarrow \infty \tag{34}$$

The values of k_W have been determined from the pressure distributions of figure 18 for values of $\frac{c}{\beta a}<4$ and from equation (34) for values of $\frac{c}{\beta a}>4$. The effect of the wing tips has been taken into account by utilizing reference 13. The results are shown in figure 22 wherein k_W is given as a function of $\frac{c}{\beta a}$ for various effective aspect ratios of 2 and greater. It should be borne in mind that the results of the figure are for a combination of body and rectangular wing or an all-movable, rectangular control surface with no gap. It is noted in the figure that the exact results for $\frac{c}{\beta a}<4$ can be faired into the asymptotic results for $\frac{c}{\beta a}>4$, thereby providing a design chart for engineering purposes for the entire range of $\frac{c}{\beta a}$. The curves of figure 22 illustrate the decrease of k_W as $\frac{c}{\beta a}$ increases at constant effective aspect ratio, and the slow increase of k_W toward unity as the wing chord becomes very large. The loss of lift is most serious for $\beta A = 2$, being about 15 percent in the worst case.

A practical point in connection with the loss of lift on the wing due to interference is that this loss occurs no matter what the body angle of attack, even though the calculations are made for $\alpha_B = 0$. It occurs either in the case of a wing mounted on a body or in the case of a deflected all-movable control surface. For wings with swept leading edges for which all of the wing area lies in the region affected by the interference, even larger losses than occur with rectangular wings are to be anticipated. However, the loss of lift at the design condition can, at least in principle, be largely prevented by designing the fuselage so that it conforms to the first Fourier component in the wing-alone flow. This would involve contracting the fuselage above the horizontal plane of symmetry in a rotationally symmetric fashion and expanding a like amount beneath the horizontal plane of symmetry. Whether or not such a change would improve the lift-drag ratio can best be determined by experiment.

Center of Pressure

The center-of-pressure locations have been calculated for the same condition as the lift results of figure 22. The center-of-pressure location in chord lengths behind the leading edge are presented in figure 23. For large values of $c*$, an asymptotic result has been calculated for $x_{c.p.}/c$ using the methods of Laplace transform theory and considering only one Fourier component.

$$\frac{x_{c.p.}}{c} \sim \frac{\frac{1}{2} - \frac{1}{3\beta A} - \left[\frac{\log 2c^*}{2c^{*2}} + \frac{2}{\pi c^*} - \frac{1}{\beta A c^{*3}}\left(1 + \frac{c^*\beta A}{2}\right)\log\left(1 + \frac{c^*\beta A}{2}\right)\right]}{k_W\left(1 - \frac{1}{2\beta A}\right)} \quad \text{as } c^* \rightarrow \infty \qquad (35)$$

The values of $\frac{x_{c.p.}}{c}$ have been determined from the pressure distributions of figure 18 for values of $\frac{c}{\beta a} < 4$ and by equation (35) for values of $\frac{c}{\beta a} > 4$. The loss of lift near the tips has been taken into consideration. The exact results for $\frac{c}{\beta a} < 4$ have been faired into the asymptotic results for large values of $\frac{c}{\beta a}$ by dashed curves to provide an engineering design chart covering the entire range of $\frac{c}{\beta a}$. It is again mentioned that this chart is applicable both to the wing of an airplane or missile or to an all-movable, rectangular control surface with no gap. The curves of figure 23 start at values of $\frac{x_{c.p.}}{c}$ corresponding to those for the wing alone at $\frac{c}{\beta a} = 0$. As $\frac{c}{\beta a}$ increases for constant βA there is a forward movement of the center of pressure because of the loss of lift due to interference which is mostly effective on the rear of the wing. For the lowest effective aspect ratio of 2 there is about a 4-percent forward movement of the center of pressure due to interference in the extreme case. For large effective aspect ratios the forward movement is not nearly so large. As the value of $\frac{c}{\beta a}$ increases for constant βA there is an asymptotic approach of the center of pressure back to the wing-alone value.

Drag

The results of the lift calculations can be used directly to determine the effect of interference on the wave drag at zero angle of attack of a symmetrical, double-wedge, rectangular wing mounted on a circular cylinder. In fact, it is not difficult to derive the result that this drag coefficient based on the area of the exposed wing is given simply as

$$\frac{\beta C_D}{(t/c)^2} = 8\left(1 - \frac{1}{4\beta A}\right)k_W\left(2\beta A, \frac{c*}{2}\right) - 4\left(1 - \frac{1}{2\beta A}\right)k_W(\beta A, c*) \qquad (36)$$

Equation (36) is for the maximum-thickness position at the midchord, although other maximum-thickness positions can easily be handled.

The values of the drag parameter given by equation (36) have been calculated for effective aspect ratios of 2, 3, and 4 using the values of k_W from figure 22. The results of the calculations are shown in figure 24 wherein $\frac{\beta C_D}{(t/c)^2}$ is plotted against $\frac{c}{\beta a}$ for constant values of βA. At $\frac{c}{\beta a} = 0$ $\frac{\beta C_D}{(t/c)^2}$ is equal to the wing-alone value of 4.

As $\frac{c}{\beta a}$ increases, there is an increase in drag which in the extreme case amounts to about 4 percent for $\beta A = 2$, and thereafter there is a steady decrease in drag until at $\frac{c}{\beta a} = 12$, the upper range of the calculations, there is about a 4-percent decrease in drag from the wing-alone value. For other effective aspect ratios the changes are inversely proportional to the effective aspect ratio. It can thus be said for rectangular wings of the present type with $\beta A > 2$ and $\frac{c}{\beta a} \leq 12$ that no important effects of interference on the minimum drag occur. For missile-like configurations for which the wing contributes only a small part of the drag, the effects of interference on minimum drag will be negligible. For wing-body combinations having a large part of the wing lying behind the Mach waves from the leading edge of the wing-body junctures, there can be appreciable effects of interference on minimum wave drag.

CONCLUDING REMARKS

A theoretical method has been developed that makes it possible to obtain the pressure field acting on a wing-body combination composed of a wing with supersonic leading and trailing edges and a circular body. The method has been applied to the calculation of the pressure fields acting on combinations of bodies and rectangular wings with the bodies at zero angle of attack. The exact calculations are for combinations for which the effective aspect ratio of the exposed wing panels joined together is greater than 2, and for which the effective chord-radius ratio is 4 or less. For the family of combinations for which the effective chord-radius ratio is 4, it was found that the blanketed area of the wing acts effectively at zero angle of attack and served primarily to support lift carried over from the wing onto the body. It was determined that for this family of combinations the body was somewhat less than 50 percent effective, compared to a perfect reflection plane, in reflecting pressure waves back onto the wing.

By comparing the contributions to the span loading of the various Fourier components, it was determined that for rectangular wing-body combinations with effective chord-radius ratios of 4 or greater, the loss of lift due to interference is associated principally with the first component. On the basis of this fact it is possible to obtain simple asymptotic formulas for wing lift and wing center-of-pressure positions for large values of the effective chord-radius ratio. The results of the exact calculations and of those based on the asymptotic formulas enabled the construction of design charts showing the wing lift and center-of-pressure position as a function of effective aspect ratio and effective chord-radius ratio. These charts are applicable to wings or control surfaces deflected in the presence of a round body. The charts show that as a result of interference the lift of the wing panels in combination can be reduced as much as 15 percent from that of the half-wings joined together, and that the center of pressure of the wing can move forward as much as 4 percent of the chord. No large effects of interference on the wave drag of symmetrical double-wedge rectangular wings with the maximum thickness at the midchord were found.

Ames Aeronautical Laboratory,
National Advisory Committee for Aeronautics,
Moffett Field, Calif., January 8, 1952.

APPENDIX A

DETERMINATION OF FUNDAMENTAL SOLUTIONS FOR FOURIER COMPONENT COMBINATIONS

Von Kármán and Moore determine the potential for a body of revolution by distributing along the axis of the body fundamental solutions of an axially symmetric type. This naturally suggests the use of fundamental solutions varying as $\cos 2n\theta$ for the Fourier component combinations for which the potential varies as $\cos 2n\theta$. Such fundamental solutions satisfy the boundary condition given by equation (5). The boundary condition given by equation (6) can be satisfied by making the fundamental solution imaginary in the forecone, that is, by making it proportional to $[(x-\xi)^2-r^2]^{m/2}$ where m is an odd integer. These conditions make the desired fundamental solutions of the form

$$\cos 2n\theta\ [(x-\xi)^2-r^2]^{m/2}\ \psi(x-\xi,r)$$

where $\psi(x-\xi,r)$ is a function to be determined in such a manner that the fundamental solution obeys the wave equation. The parameter ξ is the position on the x axis where the fundamental solution is located. In the case of a wing-body combination, ξ will vary from -1 to $+\infty$. However, a value of $\xi = 0$ is used in the derivation of the fundamental solution so that it will be at the origin. If, as a simple possibility, $\psi(x,r)$ is taken as a power of r (or x) and the fundamental solution is substituted into the wave equation in cylindrical coordinates (see fig. 1 for coordinate system)

$$\varphi_{rr} + \frac{1}{r}\varphi_r + \frac{\varphi_{\theta\theta}}{r^2} - \varphi_{xx} = 0 \tag{A1}$$

two possible sets of fundamental solutions are obtained

$$\cos 2n\theta\ \frac{(x^2-r^2)^{2n-\frac{1}{2}}}{r^{2n}} \tag{A2}$$

$$\cos 2n\theta\ \frac{r^{2n}}{(x^2-r^2)^{2n+\frac{1}{2}}} \tag{A3}$$

The first solution is singular along the body axis ($r = 0$), and the second solution is singular along the Mach cone ($x = r$). Derivatives of the above solutions with respect to x are again possible fundamental solutions.

A set of fundamental solutions having its singularities along the body axis would be better than a set having its singularities on the

Mach cone since it was desired to get the external flow field about a combination. However, when the foregoing fundamental solutions with the singularities on the axis were used, it was discovered that the functions defining the strengths of the distributions along the body axis had unmanageable singularities. In fact, only by using the (2n-1)'th derivative with respect to x of these solutions was another set of fundamental solutions obtained which gave manageable singularities in the strengths of the distributions along the axis. The set of fundamental solutions, $\varphi_{2n}{}^*(x,r,\theta)$,

$$\varphi_{2n}{}^*(x,r,\theta) = \frac{\cos 2n\theta}{r^{2n}} \frac{\partial^{2n-1}}{\partial x^{2n-1}} (x^2-r^2)^{2n-\frac{1}{2}} \tag{A4}$$

are those adopted for this report. For $n = 0$, the partial differentiation convention of equation (A4) is taken to indicate an integration with regard to x.

APPENDIX B

DETERMINATION OF AXIAL STRENGTH FUNCTIONS FOR FOURIER COMPONENT COMBINATIONS

The distribution along the axis of the fundamental solution is determined by the boundary condition of equation (9), that is, the distribution is to produce a given velocity amplitude function $f_{2n}(x)$. If the distribution of $\varphi_{2n}{}^*(x,r,\theta)$ (equation (A4)) along the body axis from -1 to ∞ to produce a step function of $f_{2n}(x)$ were known, then the axial strength distribution to produce the given function $f_{2n}(x)$ could be closely approximated by step functions as shown in figure 25. Let $h_{2n}(x-1)$ be the distribution along the axis from -1 to ∞ to produce a unit step in $f_{2n}(x)$ at the origin. Then to obtain the axial strength function to produce the stepwise approximation to $f_{2n}(x)$ shown in the figure, the following sum must be formed:

$$\sum_{j=o} h_{2n}\left(x-x_{j+1}-1\right) f_{2n}'\left(\frac{x_j+x_{j+1}}{2}\right) \Delta x_{j+1}$$

If $g_{2n}{}^*(x-1)$ is the strength distribution along the axis for the actual $f_{2n}(x)$ distribution found by letting the Δx's approach zero, then since $f_{2n}(0) = 0$

$$g_{2n}{}^*(x-1) = \int_0^x h_{2n}(x-1-\xi) f_{2n}'(\xi)\, d\xi \tag{B1}$$

with the definitions

$$g_{2n}{}^*(x-1) = g_{2n}(x) \tag{B2}$$

and

$$h_{2n}(x-1) = \frac{2^{2n}(2n!)}{(4n!)} M_{2n}(x) \tag{B3}$$

there is obtained

$$g_{2n}(x) = \frac{2^{2n}(2n!)}{(4n!)} \int_0^x M_{2n}(x-\xi)\, f_{2n}'(\xi)\, d\xi \tag{B4}$$

The changes introduced by equations (B2) and (B3) are convenient for future work. By equation (B3) the function $M_{2n}(x)$ is a simple fraction of $h_{2n}(x-1)$, the axial strength distribution necessary to produce a unit step in $f_{2n}(x)$. The functions $M_{2n}(x)$ have been studied and evaluated numerically in reference 5, and the numerical values are tabulated in table I. A plot of these functions is shown in figure 5. These functions, together with equation (B4), give a simple means of obtaining the axial strength distribution by means of numerical or graphical integration for any desired $f_{2n}(x)$. The possibility of finding universal functions $M_{2n}(x)$ for doing this is a consequence of the fact that the body is cylindrical. In the Kármán-Moore method no such simple relationship is possible because the body is of arbitrary shape.

APPENDIX C

ALTERNATE METHOD OF OBTAINING BODY PRESSURE COEFFICIENT OF FOURIER COMPONENT COMBINATION

A method of obtaining the body pressure coefficient involving only one numerical integration is now given. Consider a disturbance at the origin formed by a bump on the surface of the body as shown in figure 26. The nondimensional amplitude of the bump $\frac{f_{2n}(x)}{V}$ is to be zero except just at the origin where the area under the $f_{2n}(x)$ curve is unity, that is, the disturbance is a "delta function". The amplitude is to vary as $\cos 2n\theta$. Now if the pressure coefficient in the wing-body juncture is $-2\ W_{2n}(x)$ due to the unit disturbance at the origin, then the contribution to the pressure coefficient at a downstream distance x due to a distribution of disturbances from the origin to the point in question is

$$\delta P_{2n} = -\frac{2}{V} \cos 2n\theta \int_0^x f_{2n}(\xi) W_{2n}(x-\xi)\, d\xi \tag{C1}$$

This integral is the effect of all disturbances forward of the point and is additive to the effect of the disturbance exactly at the point. The local value is that given by the Ackeret theory, namely,

$$P = -\frac{2\alpha_l}{\sqrt{M^2-1}} \tag{C2}$$

where α_l is the local angle of attack

$$\alpha_l = \frac{f_{2n}(x)}{V} \cos 2n\theta \tag{C3}$$

The pressure coefficient due to all disturbance is thus

$$P_{2n} = \frac{2}{V} \cos 2n\theta\ f_{2n}(x) - \frac{2}{V} \cos 2n\theta \int_0^x f_{2n}(\xi) W_{2n}(x-\xi)\, d\xi \tag{C4}$$

The advantage of this method of obtaining the pressure coefficient at the body surface is that the pressure coefficient is obtained directly as a function of the boundary condition, $f_{2n}(x)$, without first determining an axial strength function.

The $W_{2n}(x)$ functions introduced to determine the body pressure distributions are universal functions that have been studied in reference 5.

They are presented in table II, and curves of them are presented in figure 7. The values of $W_0(x)$ have been tabulated by G. N. Ward in reference 11.

Several interesting facts are illustrated by figure 7. The amplitude of the pressure distribution due to a unit disturbance of the type shown in figure 26 has exactly $2n$ points of zero pressure, and these points are nearly evenly spaced. The large number of points of zero pressure for the higher harmonics makes their lift contributions much less significant than their pressure contributions. Another interesting feature of figure 7 is that the $W_{2n}(x)$ functions damp much more rapidly in the downstream direction for the higher harmonics than the lower harmonics. In fact, for $n = 0$ the damping to 4 percent of the maximum value occurs about 7 body radii downstream, whereas for $n = 5$ the same damping occurs in about 2 body radii.

REFERENCES

1. Spreiter, John R.: Aerodynamic Properties of Slender Wing-Body Combinations at Subsonic, Transonic, and Supersonic Speeds. NACA Rep. 962, 1950. (Formerly NACA TN's 1662 and 1897)

2. Browne, S. H., Friedman, L., and Hodes, I.: A Wing-Body Problem in a Supersonic Conical Flow. Jour. Aero. Sci., vol. 15, no. 8, 1948, pp. 443-452.

3. Ferrari, Carlo: Interference Between Wing and Body at Supersonic Speeds - Theory and Numerical Application. Jour. Aero. Sci., vol. 15, no. 6, 1948, pp. 317-336.

4. Nielsen, Jack N., and Matteson, Frederick H.: Calculative Method for Estimating the Interference Pressure Field at Zero Lift on a Symmetrical Swept-Back Wing Mounted on a Circular Cylindrical Body. NACA RM A9E19, 1949.

5. Nielsen, Jack N.: Supersonic Wing-Body Interference. Calif. Inst. of Tech. Doctoral Thesis, 1951.

6. von Kármán, Theodore, and Moore, N. B.: Resistance of Slender Bodies Moving With Supersonic Velocities, With Special Reference to Projectiles. Amer. Soc. Mech. Engrs., vol. 54, 1932, pp. 303-310.

7. Morikawa, George K.: The Wing-Body Problem for Linearized Supersonic Flow. Calif. Inst. of Tech. Doctoral Thesis, 1949.

8. Morikawa, George: Supersonic Wing-Body Lift. Jour. Aero. Sci., vol. 18, no. 4, 1951, pp. 217-228.

9. Tsien, H.: Supersonic Flow Over an Inclined Body of Revolution. Jour. Aero. Sci., vol. 5, no. 12, 1938, pp. 480-483.

10. Lagerstrom, P. A., and Van Dyke, M. D.: General Considerations About Planar and Nonplanar Lifting Systems. Douglas Aircraft Co., Rept. No. SM-13432, June, 1949.

11. Ward, G. N.: The Approximate External and Internal Flow Past a Quasi-Cylindrical Tube Moving at Supersonic Speeds. Quart. Jour. Mech. and App. Math., vol. I, pt. 2, June, 1948, pp. 225-245.

12. U. S. National Bureau of Standards; National Applied Mathematics Laboratories; Computation Laboratory. Tables of Lagrangian Interpolation Coefficients. Prepared by the Mathematical Tables Project, Work Projects Administration of the Federal Works Agency. Conducted under the sponsorship of the National Bureau of Standards. New York, Columbia University Press, 1944.

13. Busemann, Adolf: Infinitesimal Conical Supersonic Flow. NACA TM 1100, 1947.

TABLE I.- VALUES OF $M_{2n}(x)$

x	$M_0(x)$	$M_2(x)$	$M_4(x)$	$M_8(x)$
0	$-\infty$	$-\infty$	$-\infty$	$-\infty$
.05	----	----	-.531	-.716
.1	-1.321	-.787	.405	1.334
.15	----	----	----	1.155
.2	-.868	-.166	.902	.735
.25	----	----	----	.279
.3	----	.131	.831	-.119
.35	----	----	----	-.417
.40	-.538	.304	.560	-.595
.45	----	----	----	-.675
.50	----	----	.245	-.655
.6	-.378	.450	-.040	-.417
.7	----	----	-.253	-.070
.75	----	----	----	.095
.8	-.292	.457	-.386	.235
.85	----	----	----	.340
.9	----	----	-.434	.406
.95	----	----	----	.433
1.0	-.224	.392	-.412	.420
1.1	----	----	-.337	.306
1.2	-.180	.294	-.231	.123
1.3	----	----	-.115	-.062
1.4	-.147	.188	.000	-.197
1.5	----	----	.095	-.256
1.6	-.122	.088	.163	-.239
1.7	----	----	.204	-.162
1.8	-.102	.005	.211	-.062
1.9	----	----	.197	.036
2.0	-.086	-.058	.164	.105
2.1	----	----	----	.134
2.2	-.073	-.100	.069	.121
2.3	----	----	.020	.085
2.4	-.062	-.123	-.022	.036
2.5	----	----	-.053	-.013
2.6	-.053	-.126	-.073	-.053
2.7	----	----	----	-.063
2.8	-.045	-.119	-.080	-.059
2.9	----	----	-.071	-.042
3.0	-.038	-.103	-.060	-.019
3.1	----	----	-.038	.005
3.2	-.031	-.083	-.019	.022
3.3	----	----	-.002	.030
3.4	-.026	-.061	.011	.028
3.5	----	----	.021	.019
3.6	-.022	-.040	.027	.008
3.7	----	----	.027	-.002
3.8	-.018	-.022	.025	-.011
3.9	----	----	.022	-.014
4.0	-.016	-.007	.015	-.103

NOTE that $M_{2n}(x) \longrightarrow -\frac{1}{\pi}\sqrt{\frac{2}{x}}$ as $x \longrightarrow 0$.

TABLE II.- VALUES OF $W_{2n}(x)$

x	$W_0(x)$	$W_2(x)$	$W_4(x)$	$W_6(x)$	$W_8(x)$	$W_{10}(x)$
0	0.500	0.500	0.500	0.500	0.500	0.500
.05	----	----	----	----	----	2.787
.10	----	----	----	2.022	3.136	4.459
.15	----	----	----	----	3.884	5.264
.20	.4319	.7541	1.644	2.888	4.176	5.164
.25	----	----	----	3.037	4.021	4.213
.30	----	----	----	3.008	3.486	2.857
.35	----	----	----	----	----	1.209
.40	.3755	.878	1.929	2.462	1.702	-.345
.50	----	----	----	1.545	-.215	-2.296
.60	.3284	.892	1.428	.508	-1.458	-1.986
.70	----	----	----	----	-1.697	-.461
.80	.2887	.826	.706	-.940	-1.116	.980
.85	----	----	----	----	----	1.317
.90	----	----	----	----	-.163	1.345
.95	----	----	----	----	----	1.107
1.0	.2550	.706	-.024	-.974	.634	.676
1.1	----	----	----	----	.930	-.279
1.2	.2262	.557	-.464	-.150	.741	-.803
1.3	----	----	----	----	----	.638
1.4	.2014	.402	-.558	.457	-.213	-.045
1.5	----	----	----	----	-.479	.399
1.6	.1801	.255	-.418	.455	-.514	.475
1.7	----	----	----	----	----	.251
1.8	.1616	.128	-.142	.073	.022	-.129
1.9	----	----	----	----	----	-.297
2.0	.1454	.026	.081	-.222	.276	-.214
2.1	----	----	----	----	----	-.005
2.2	.1313	-.048	.195	-.217	.043	.154
2.3	----	----	----	----	----	.167
2.4	.1189	-.097	.196	-.035	-.173	.061
2.5	----	----	----	----	----	-.058
2.6	.1080	-.122	.120	.106	-.053	-.108
2.8	.0983	-.128	.025	.098	.075	.007
3.0	.0898	-.122	-.049	-.001	----	.058
3.2	.0822	-.104	-.078	-.043	-.049	-.066
3.4	.0754	-.082	-.068	-.050	-.030	-.017
3.6	.0693	-.058	-.035	-.008	.011	.022
3.8	.0638	-.035	-.003	.046	----	----
4.0	.0590	-.017	----	.024	----	----

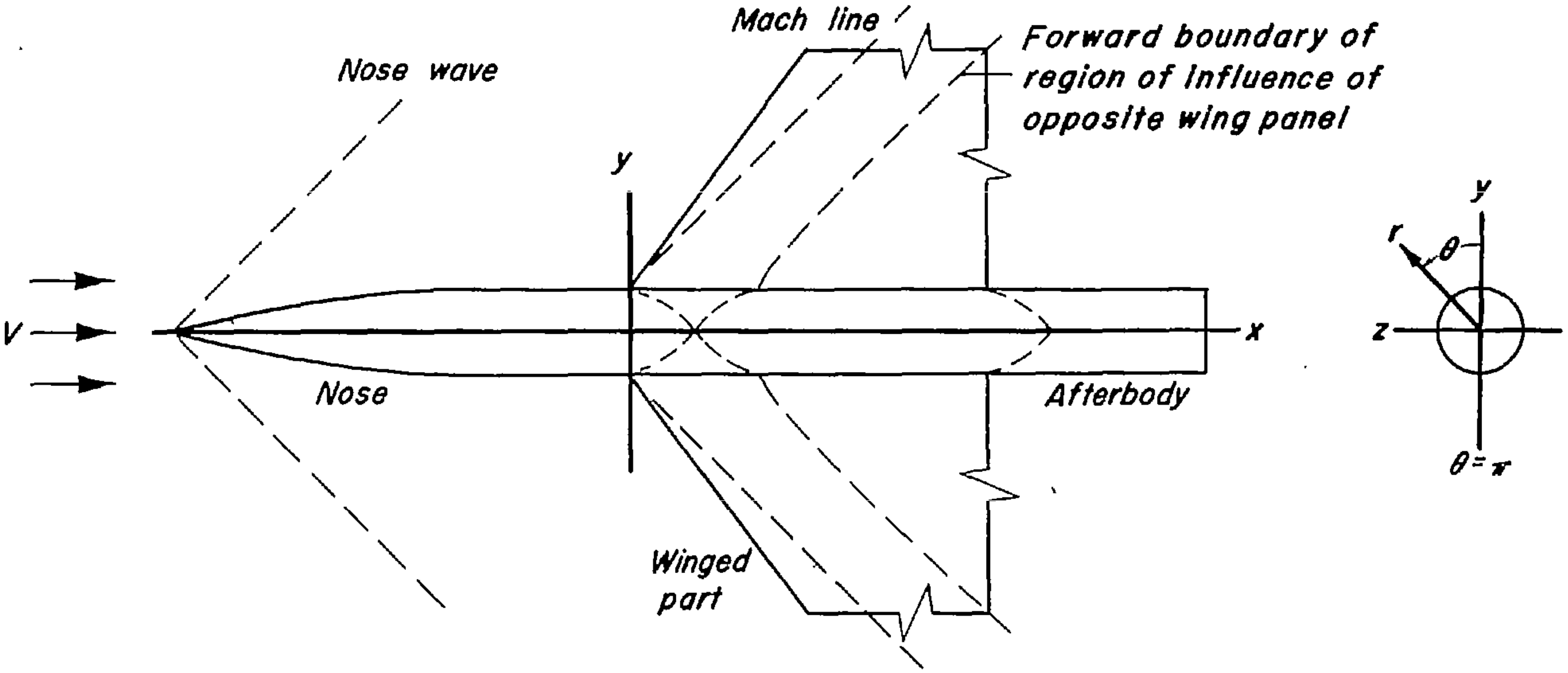
Mach line
Forward boundary of region of influence of opposite wing panel
Nose wave
y
V
x
Nose
Afterbody
Winged part
r
θ
y
z
θ = π

Figure 1.- Components of typical wing-body combination.

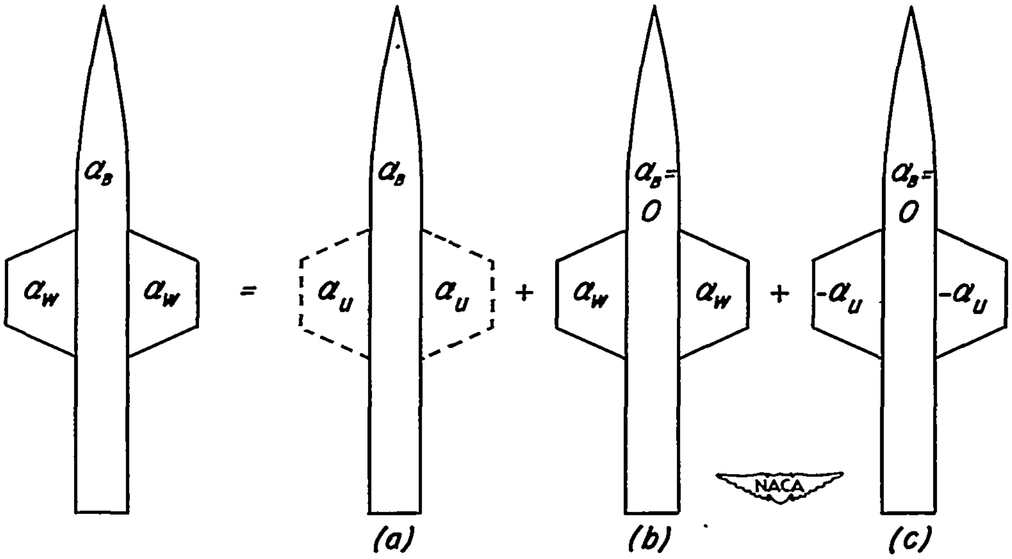

α_B
α_W
α_W
=
α_B
α_U
α_U
+
$\alpha_B = 0$
α_W
α_W
+
$\alpha_B = 0$
$-\alpha_U$
$-\alpha_U$
(a)
(b)
(c)

Figure 2.- Decomposition of wing-body combination into component configurations.

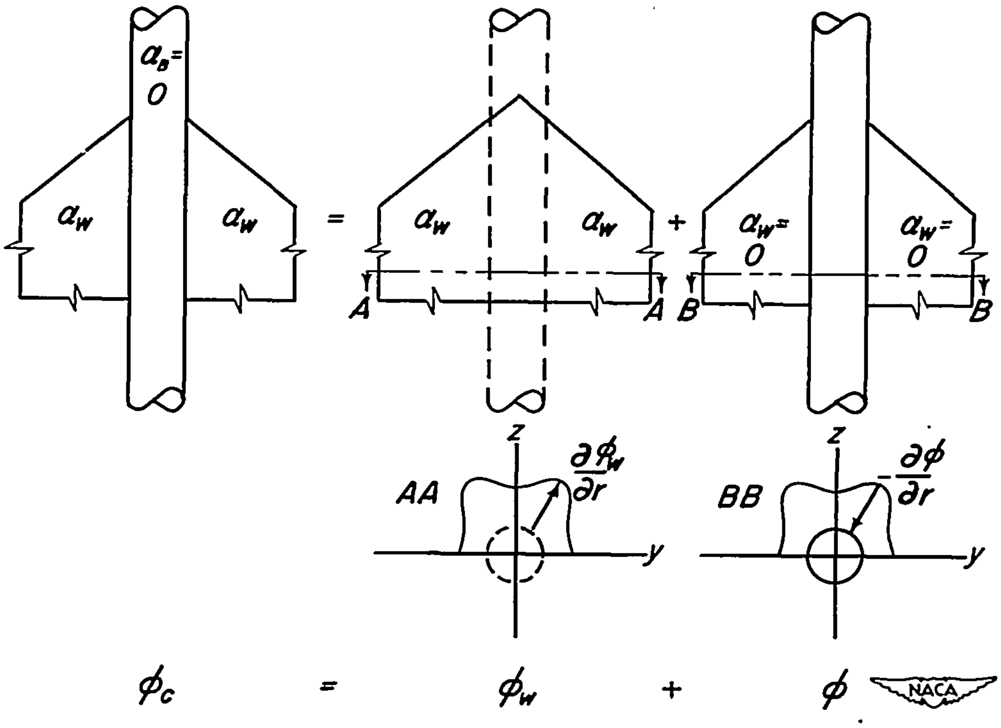

$\alpha_B = 0$
α_W
α_W
=
α_W
α_W
+
$\alpha_W = 0$
$\alpha_W = 0$
A
A
B
B
z
AA
$\frac{\partial \phi_W}{\partial r}$
y
z
BB
$-\frac{\partial \phi}{\partial r}$
y
ϕ_c
=
ϕ_W
+
ϕ

Figure 3.- Wing-body combination as the sum of wing alone plus interference combination.

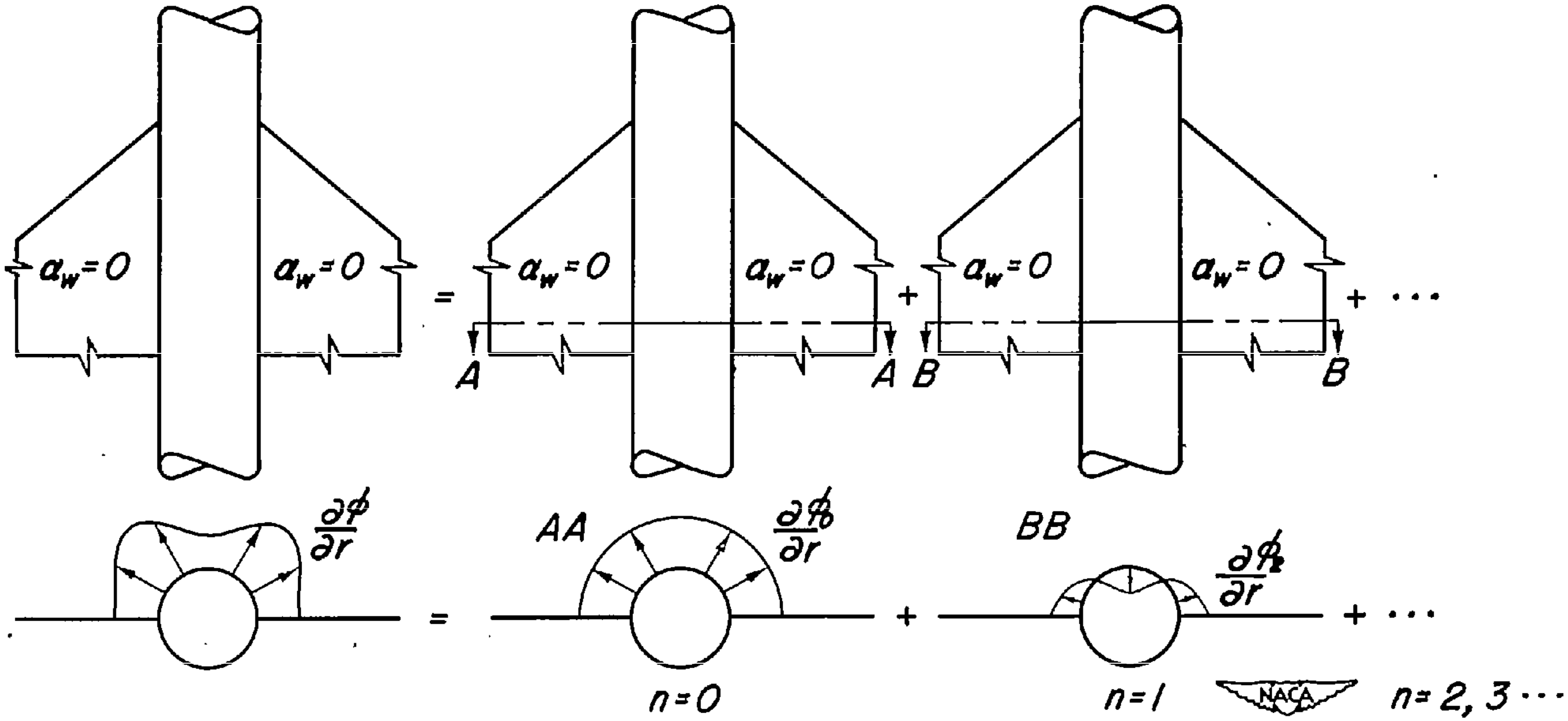
$\alpha_w = 0$
$\alpha_w = 0$
=
$\alpha_w = 0$
$\alpha_w = 0$
+
$\alpha_w = 0$
$\alpha_w = 0$
+ ...
A
A
B
B
$\frac{\partial \phi}{\partial r}$
=
AA
$\frac{\partial \phi_0}{\partial r}$
+
BB
$\frac{\partial \phi_1}{\partial r}$
+ ...
n=0
n=1
NACA
n=2, 3 ...

Figure 4.- Decomposition of interference combination into series of Fourier component interference combinations.

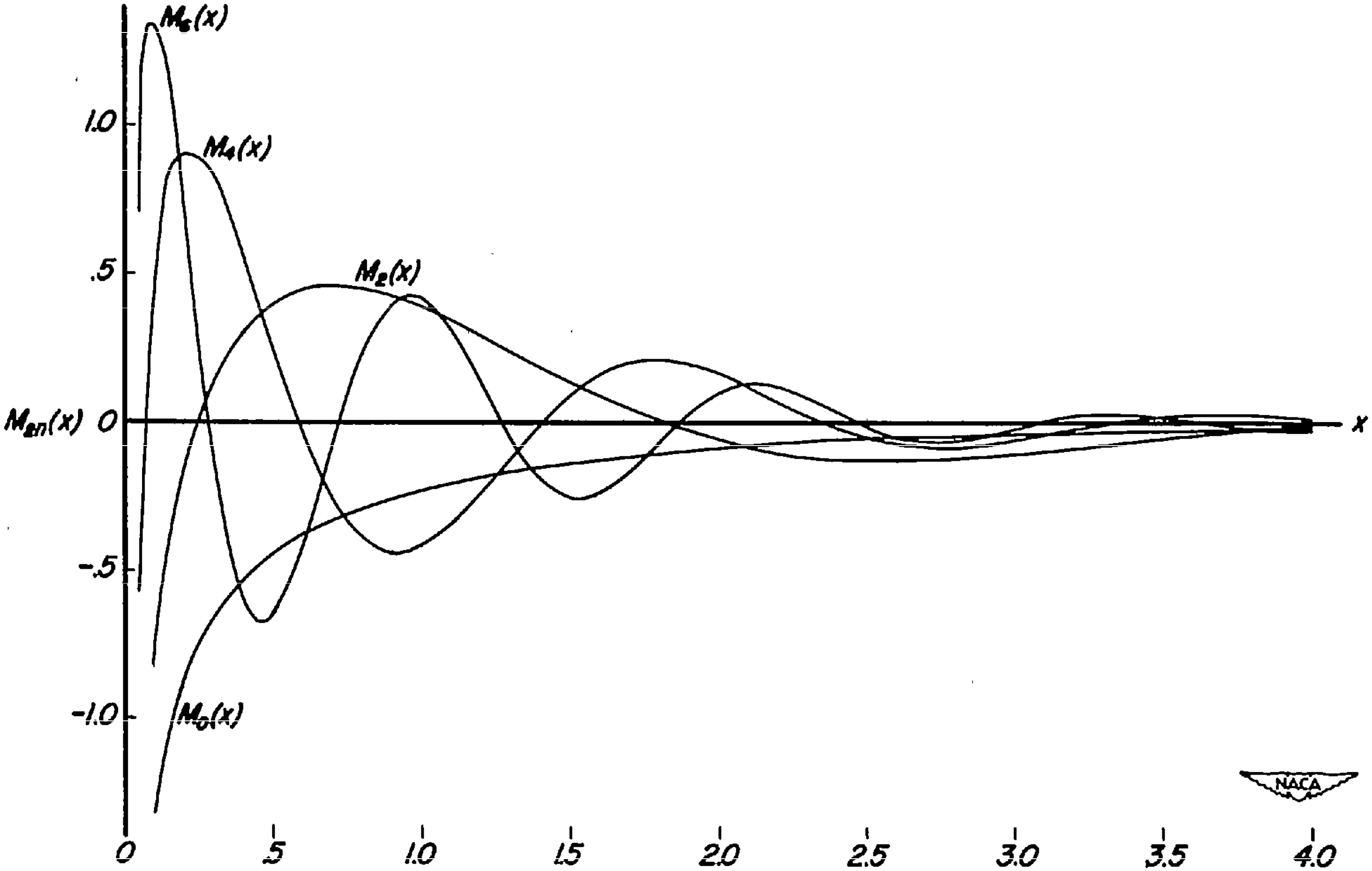

Figure 5. – Graphical presentation of $M_{2n}(x)$ functions.

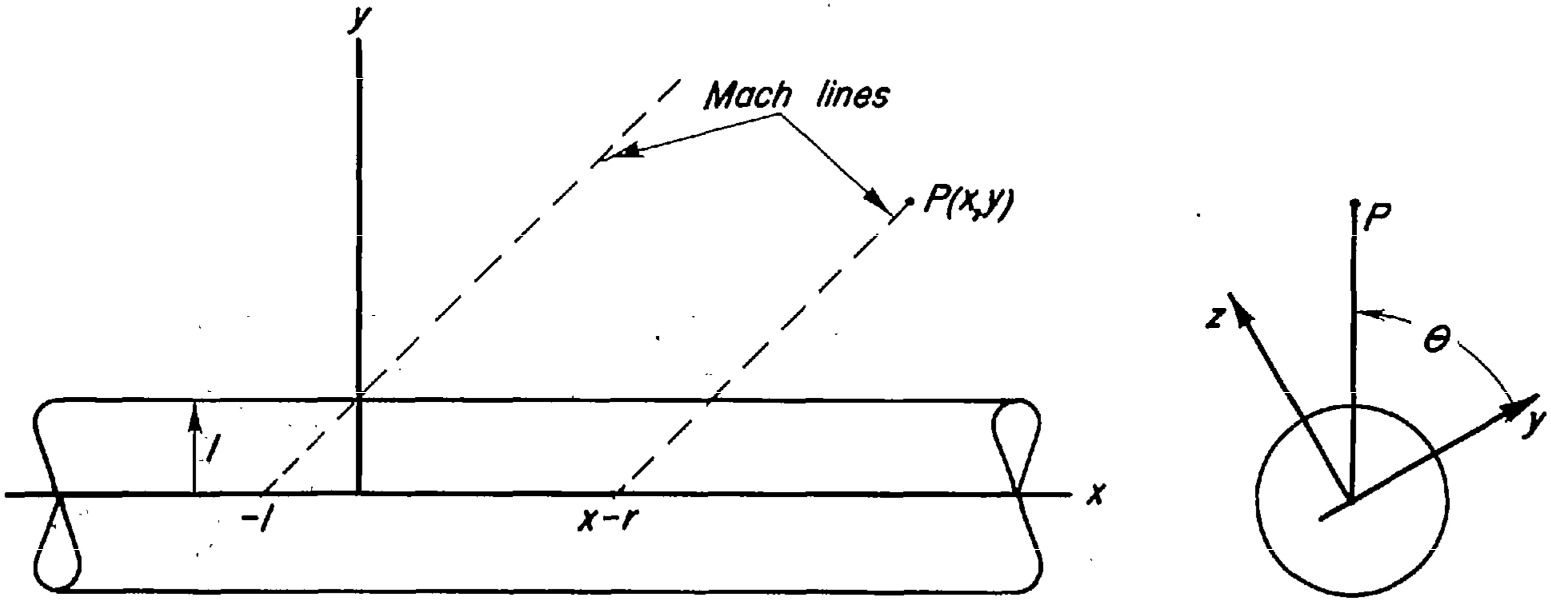
y
Mach lines
P(x,y)
l
-l
x-r
x
P
z
θ
y

Figure 6. - General point at which potential is to be determined.

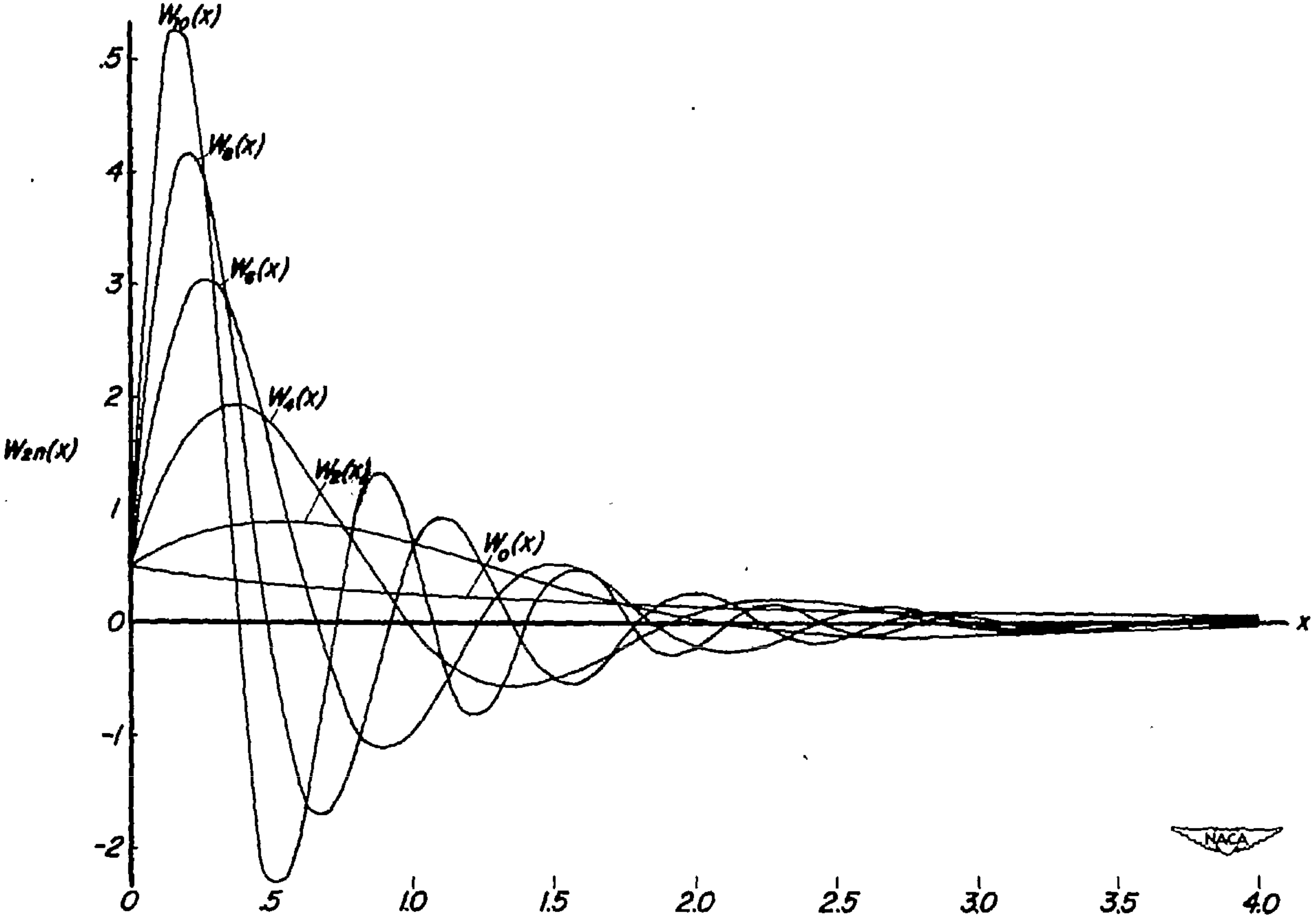

Figure 7.—Graphical presentation of $W_{2n}(x)$ functions.

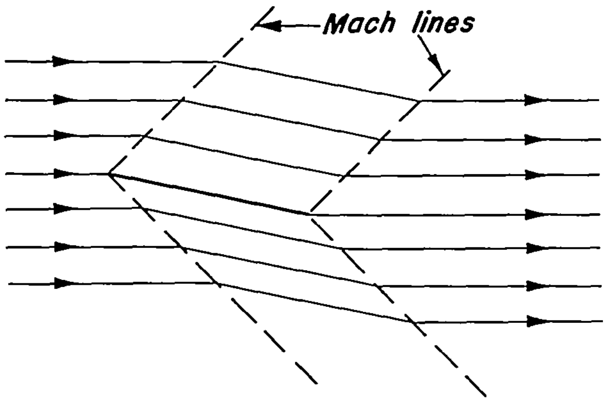

Figure 8.—Flow field produced by wing alone.

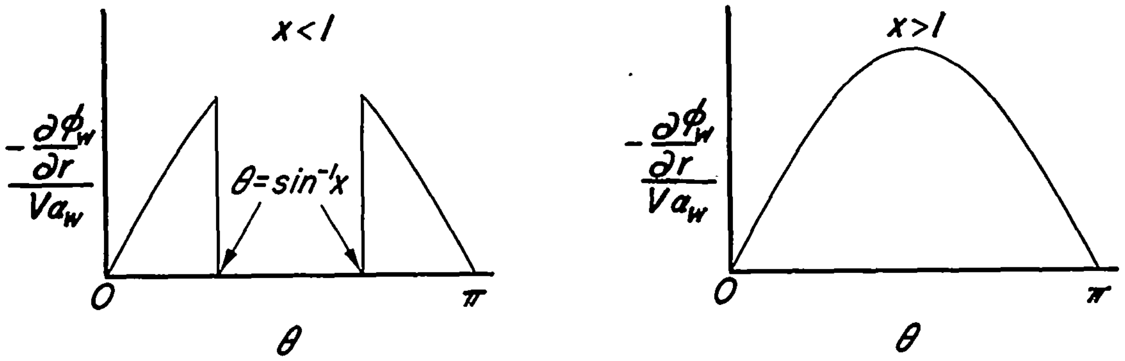

Figure 9.— Variation of normal velocity induced at body surface by wing alone, unit body radius.

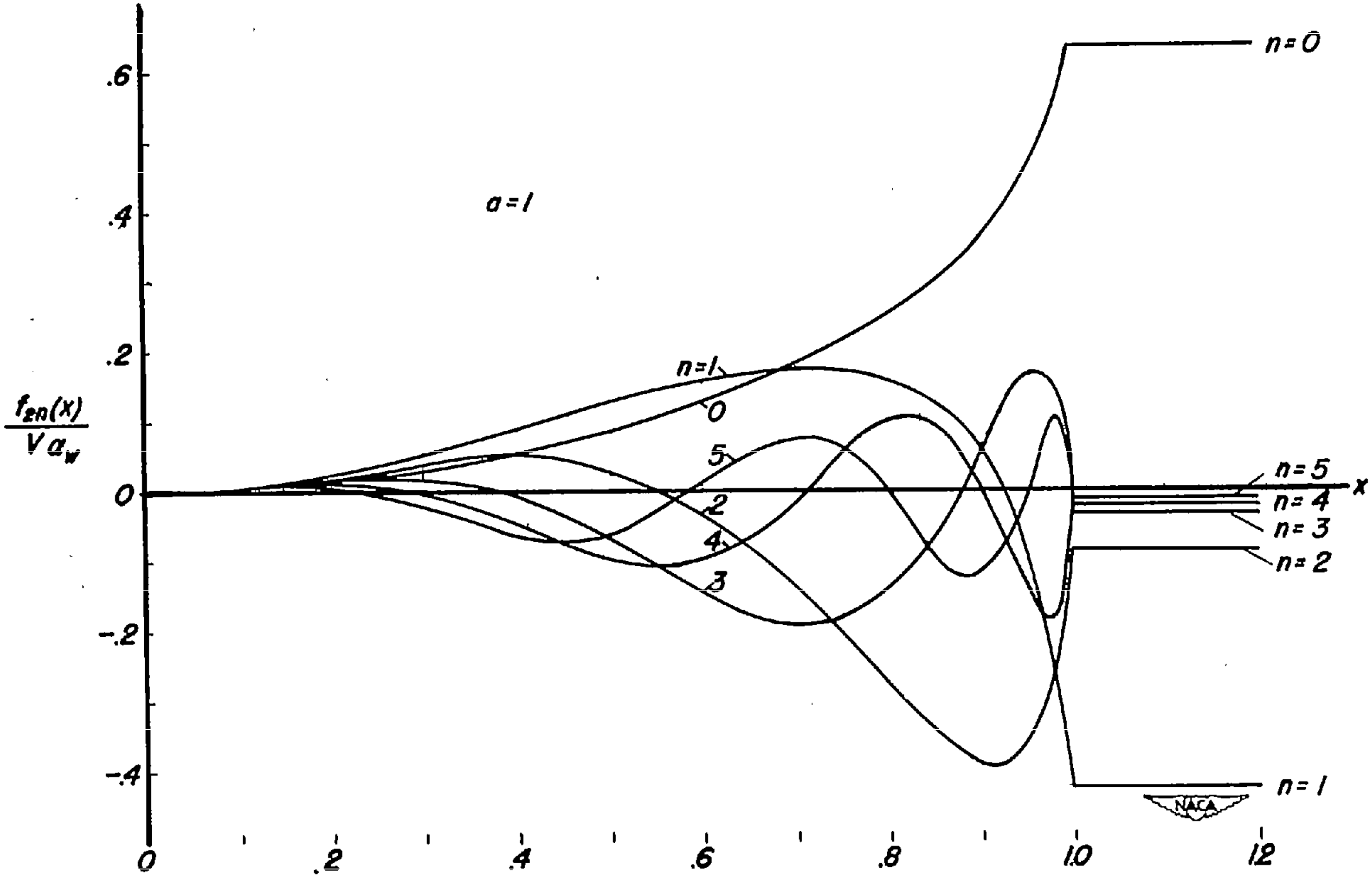

Figure 10.– Graphical representation of velocity amplitude functions.

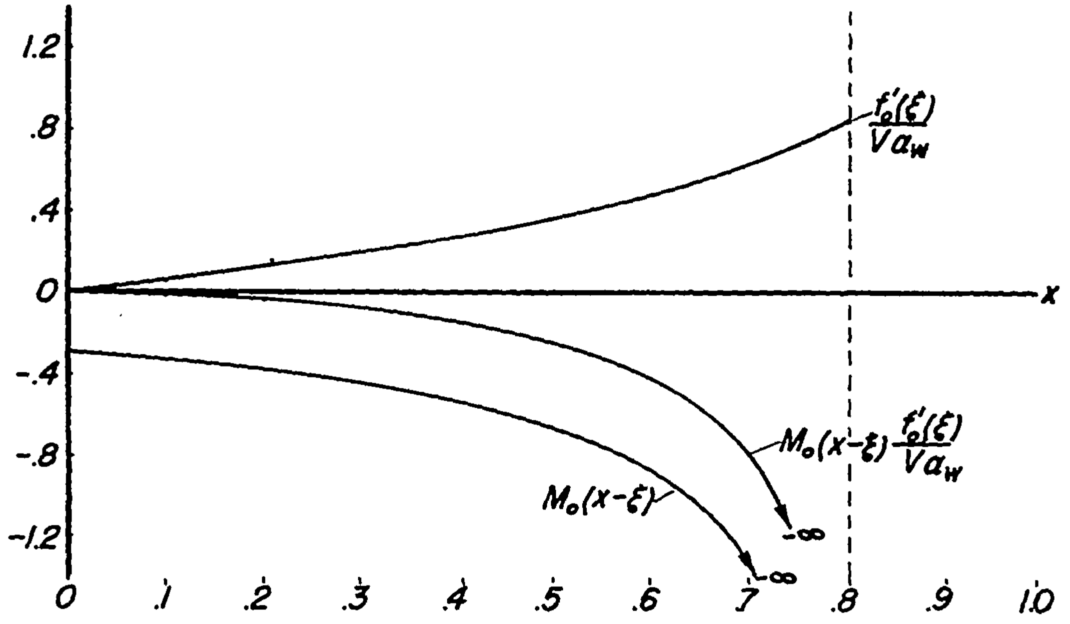

(a) $x<l$

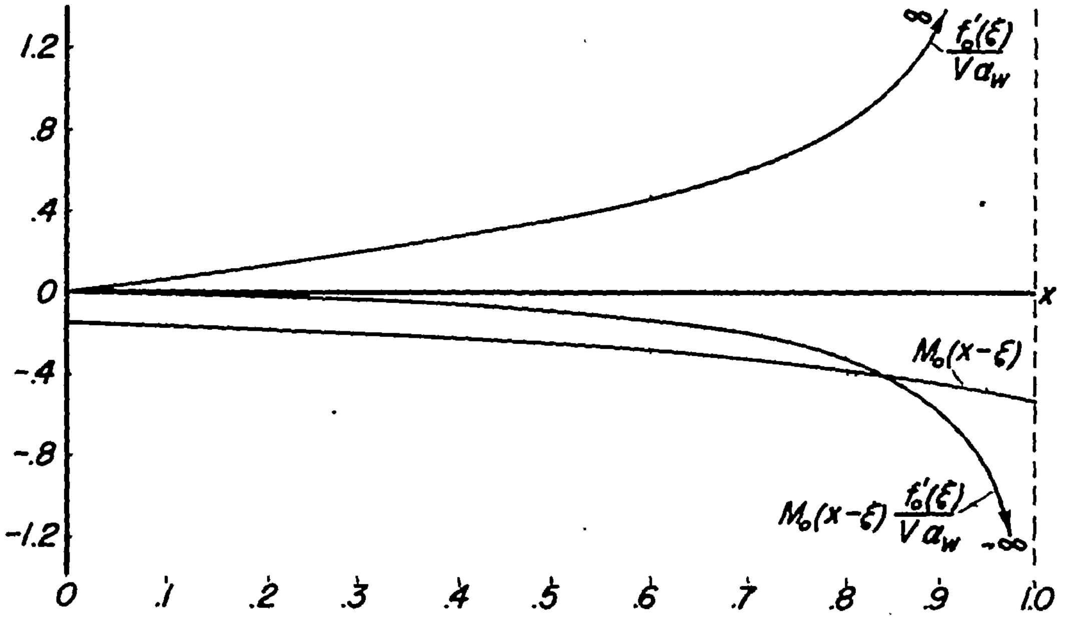

(b) $x>l$

Figure 11.- Singularities encountered in determining axial strength functions.

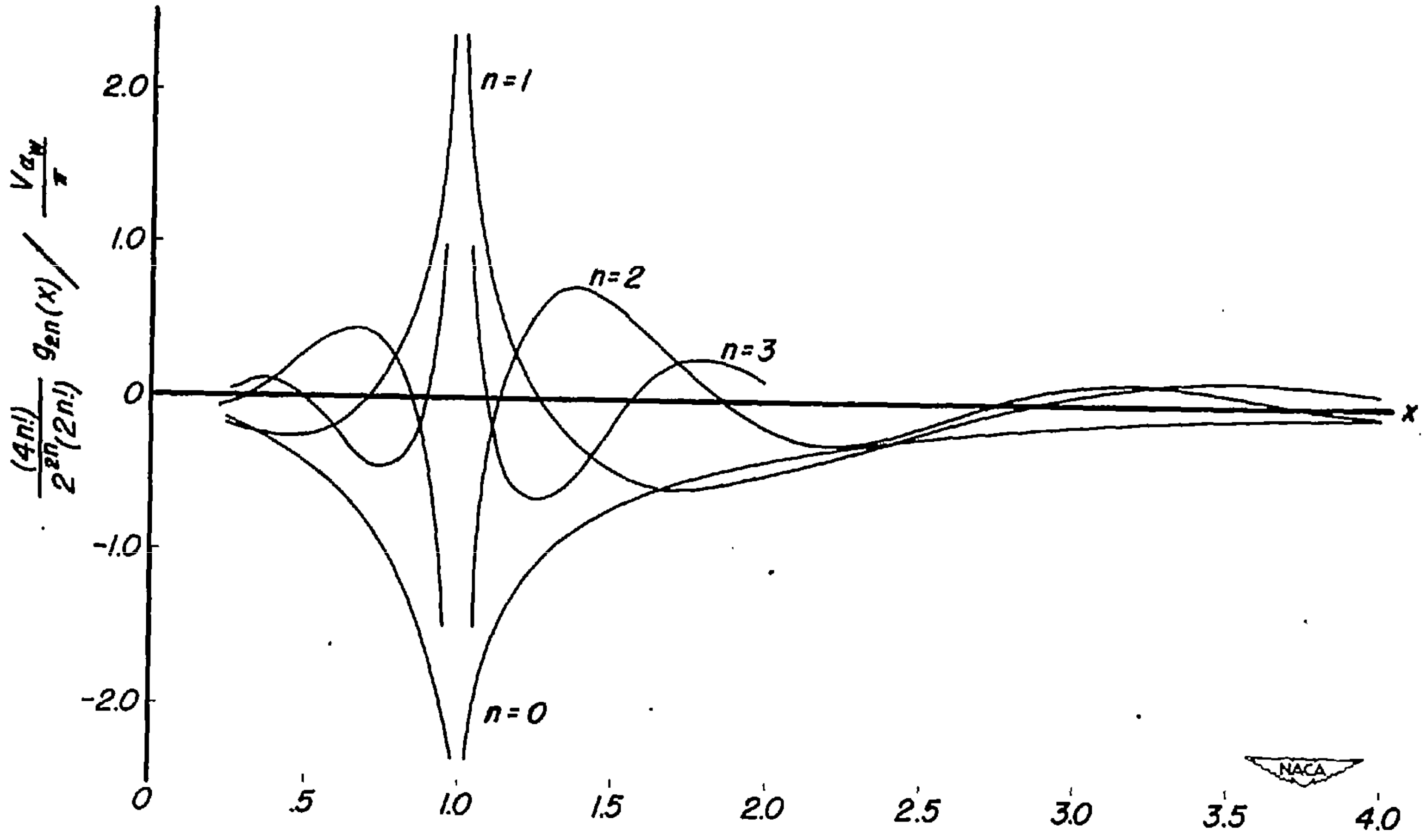

Figure 12.– Graphical presentation of axial strength functions.

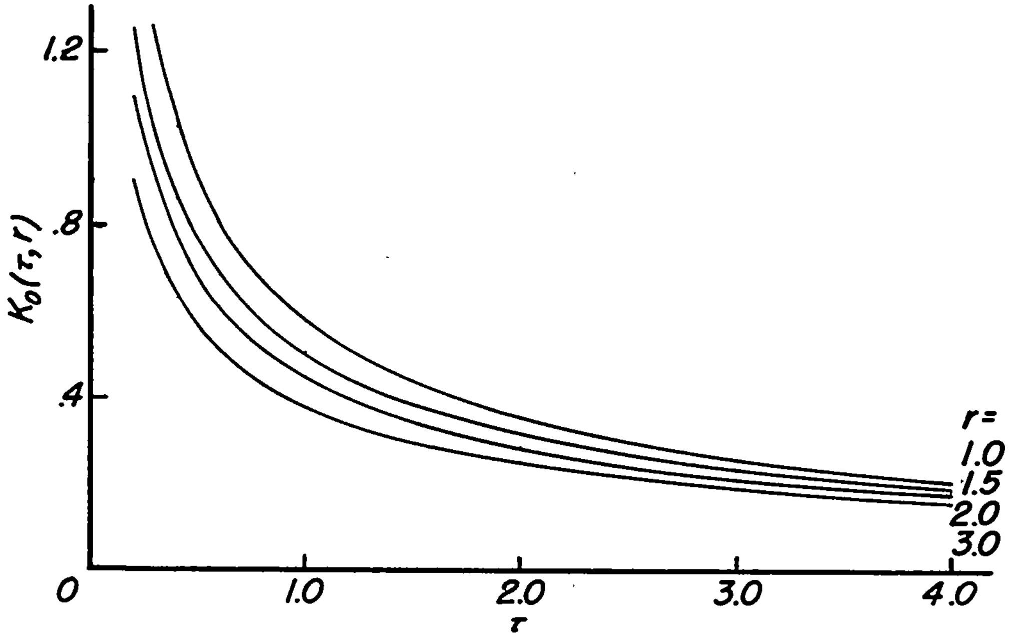

(a) $K_0(\tau,r)$

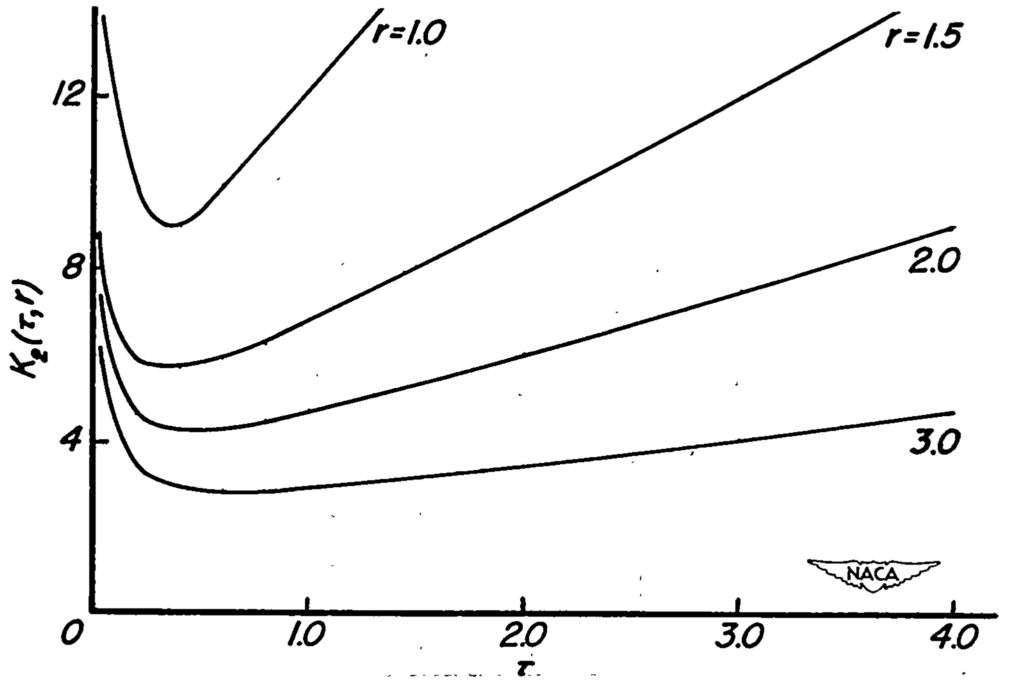

(b) $K_2(\tau,r)$

Figure 13.- Curves of $K_0(\tau,r)$ and $K_2(\tau,r)$.

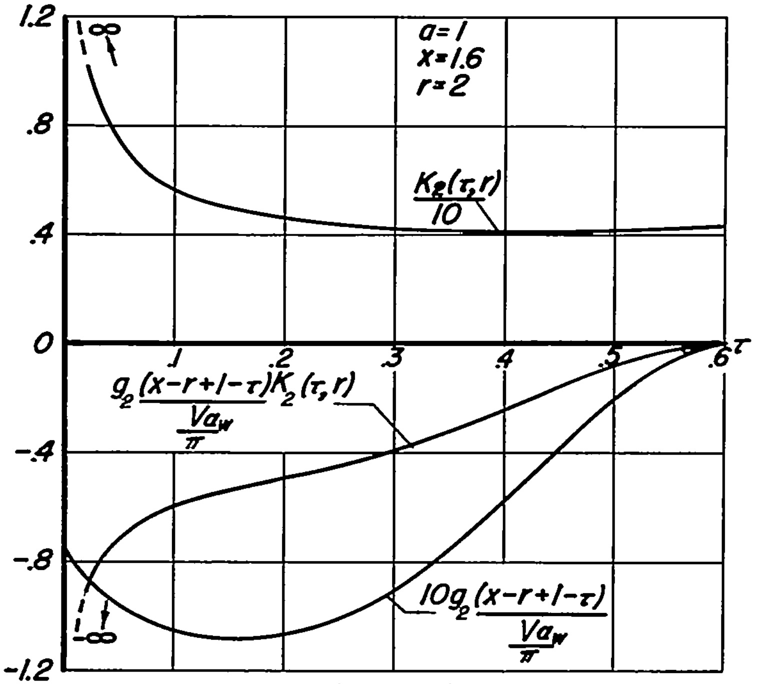

(a) $x-r+1<1$

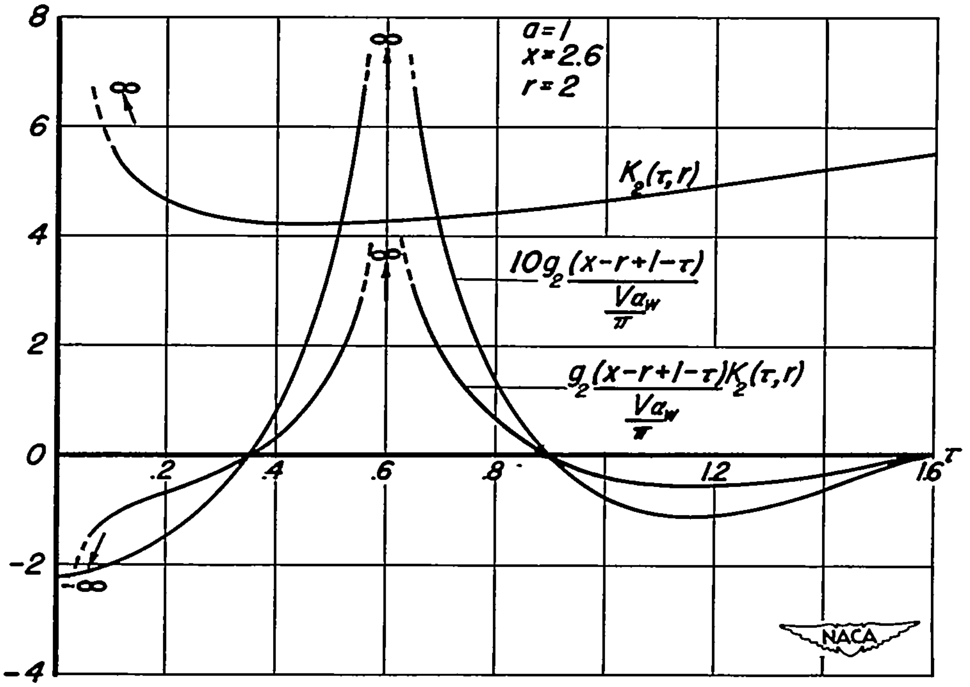

(b) $x-r+1>1$

Figure 14 - Singularities encountered in determining interference pressure coefficients.

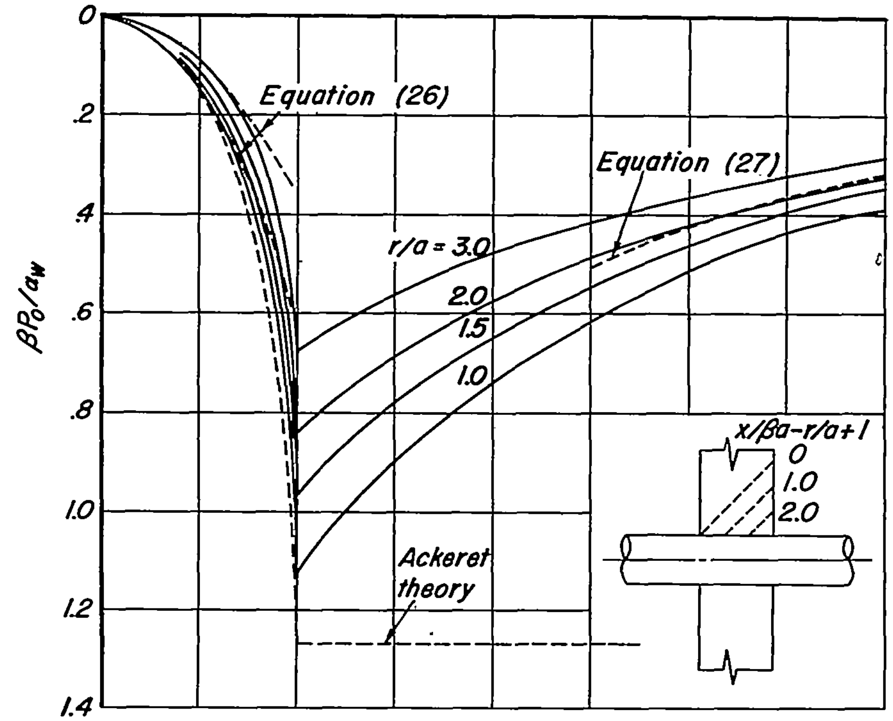

(a) n=0

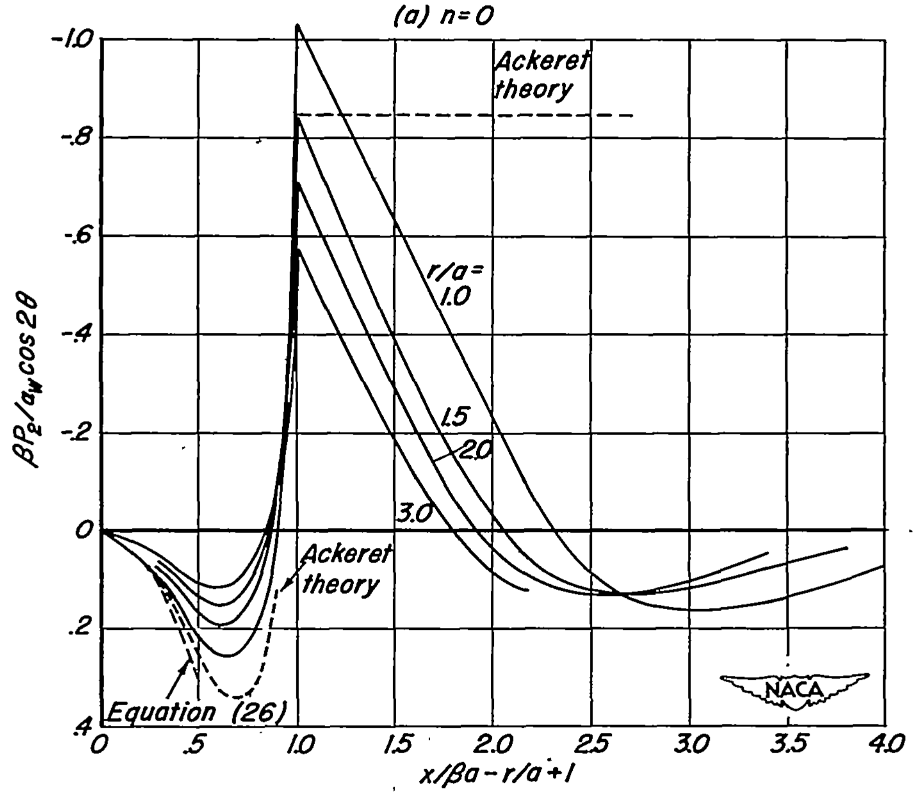

(b) n=1

Figure 15.- Interference pressure distributions of various Fourier components.

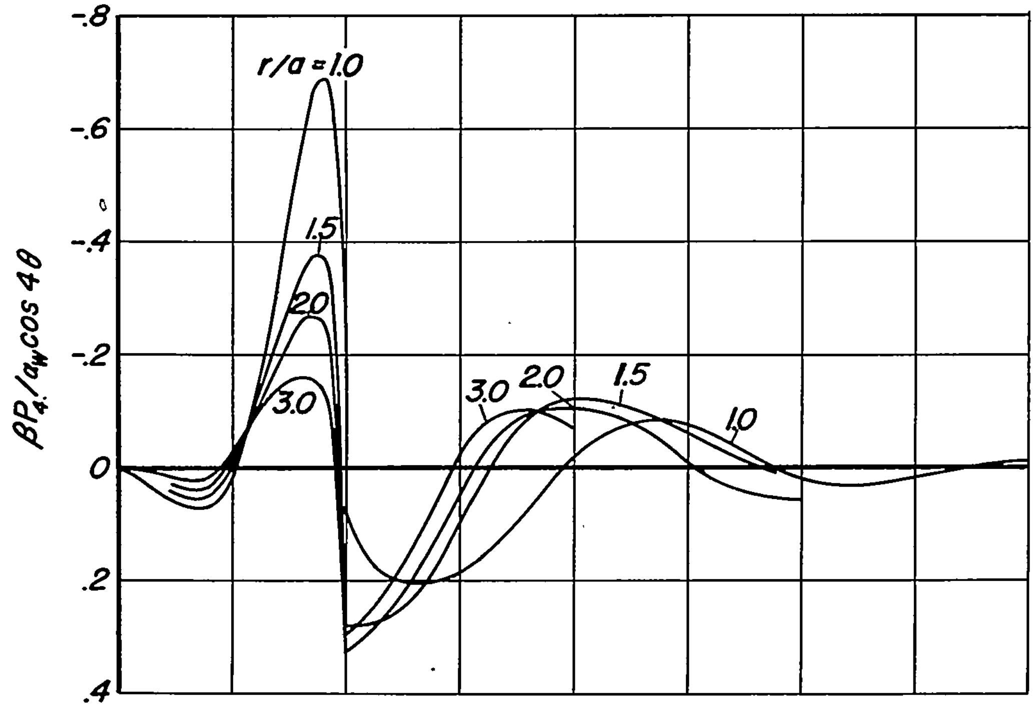

(c) n = 2

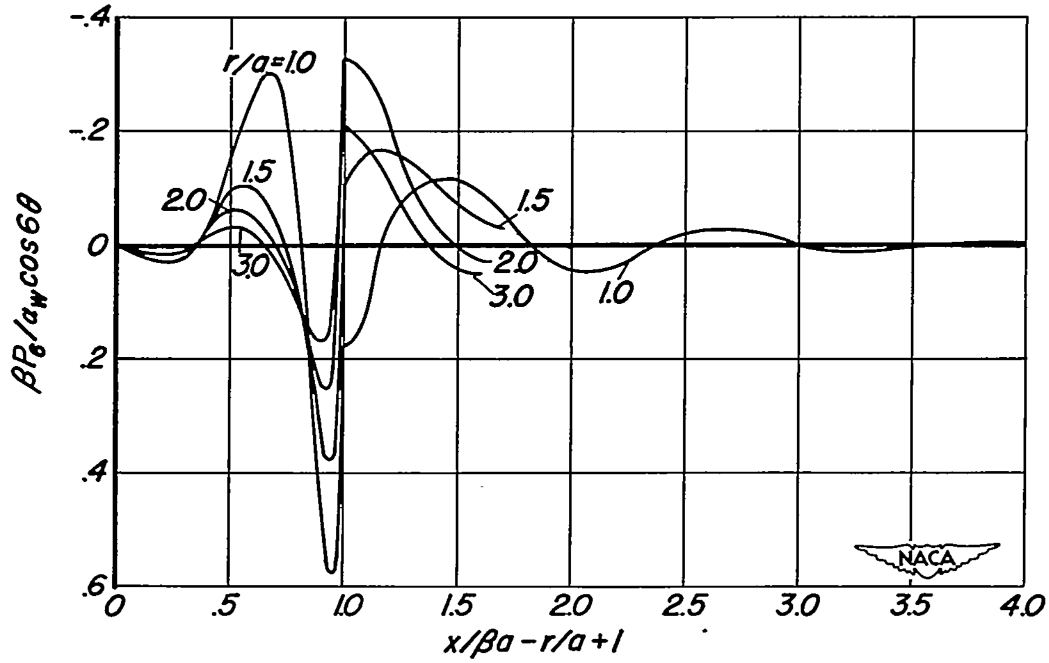

(d) n = 3

Figure 15.- Concluded.

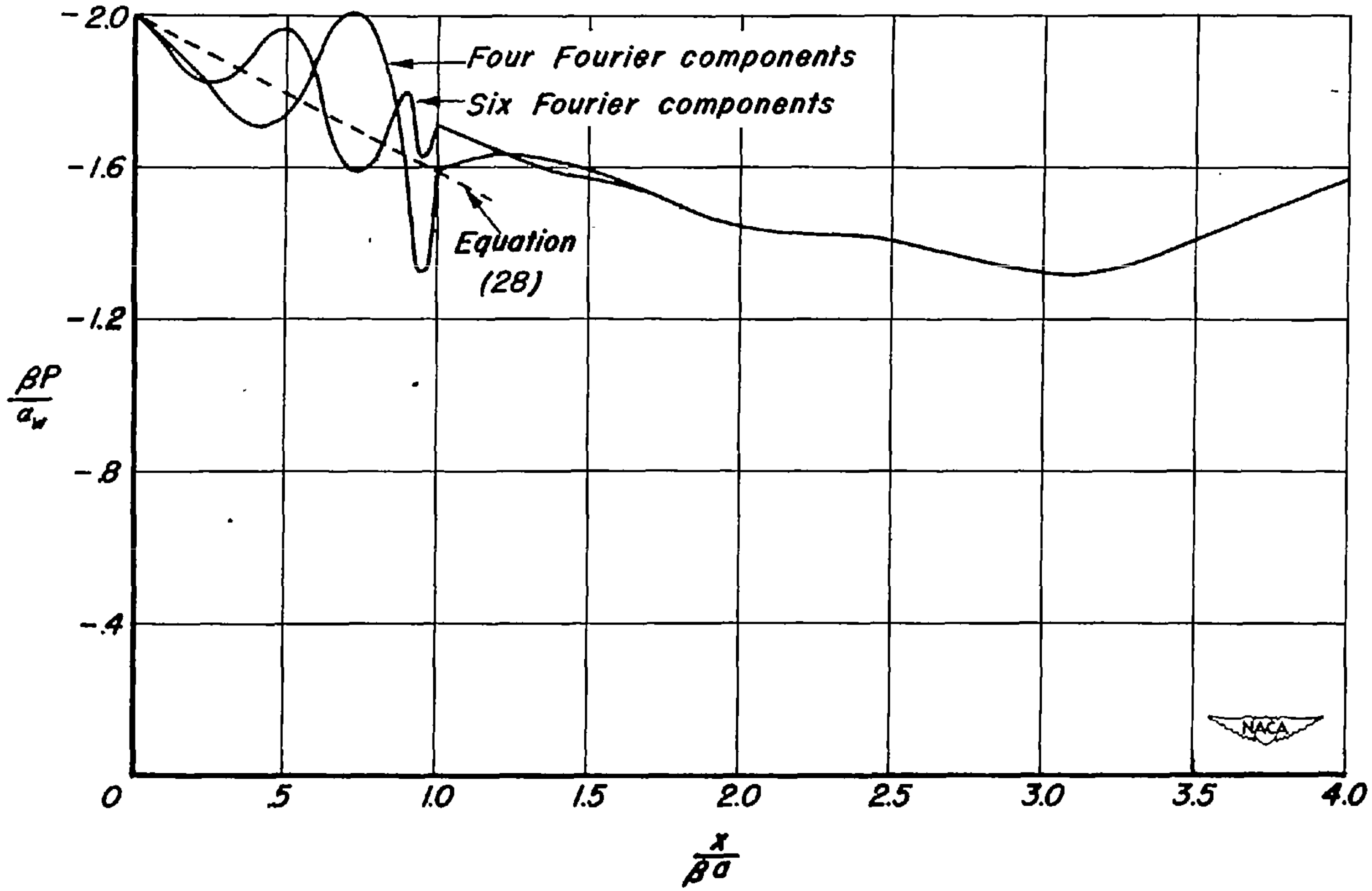

Figure 16.- Pressure distribution at wing-body juncture of combination of body and rectangular wing using four and six Fourier components.

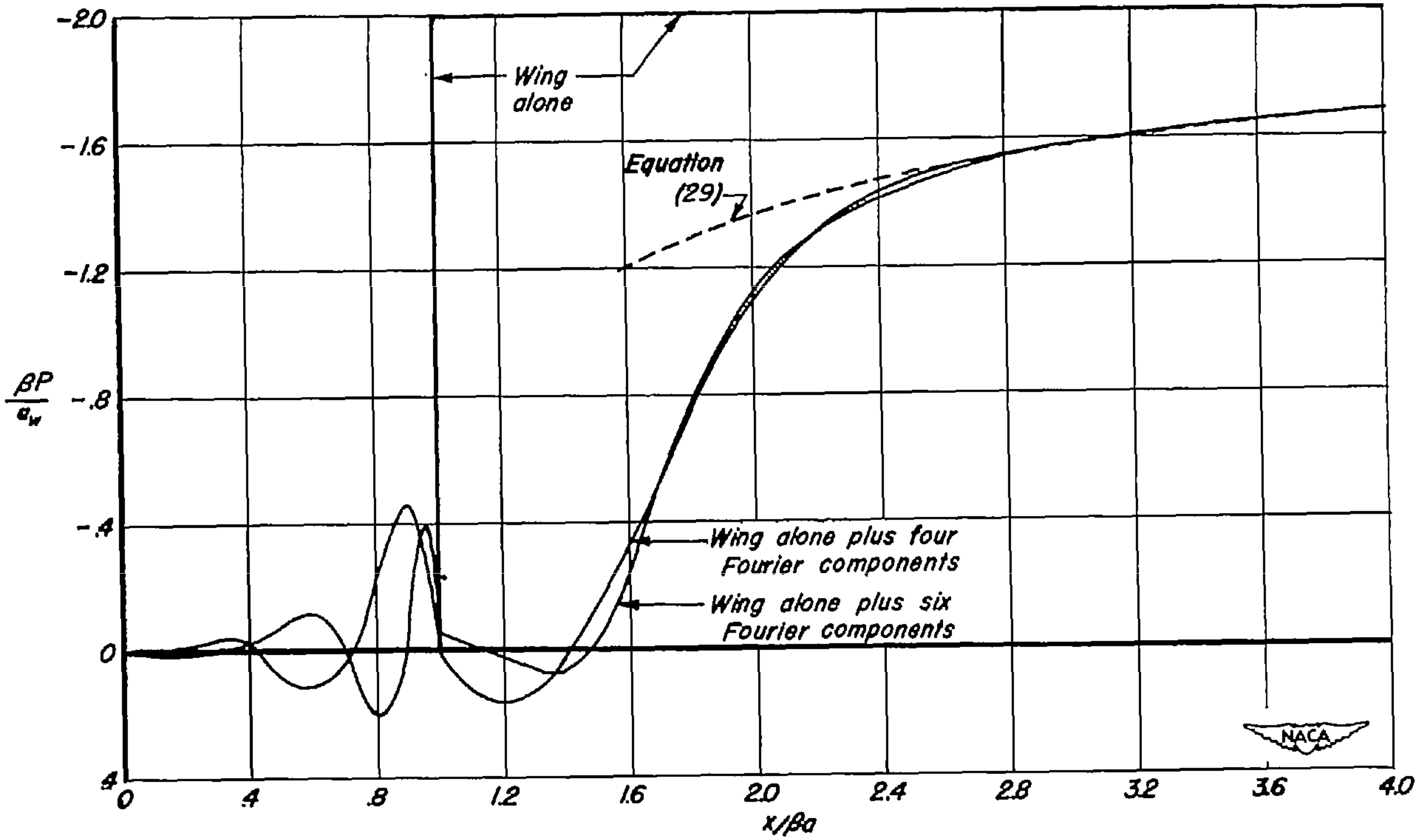

Figure 17. – Pressure distribution on top of combination of body and rectangular wing using four and six Fourier components.

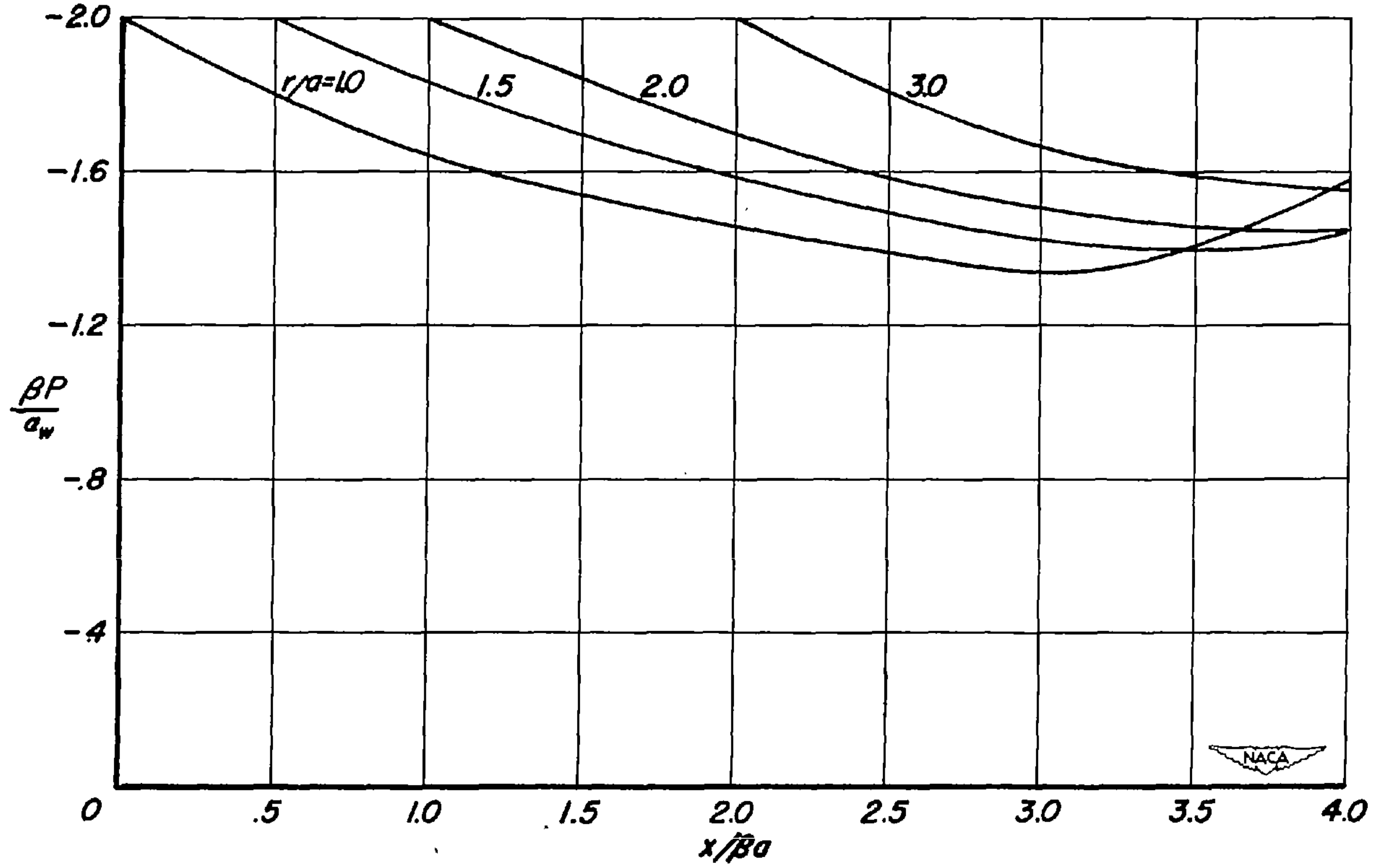

Figure 18.—Pressure distribution acting on wing of combination of body and rectangular wing.

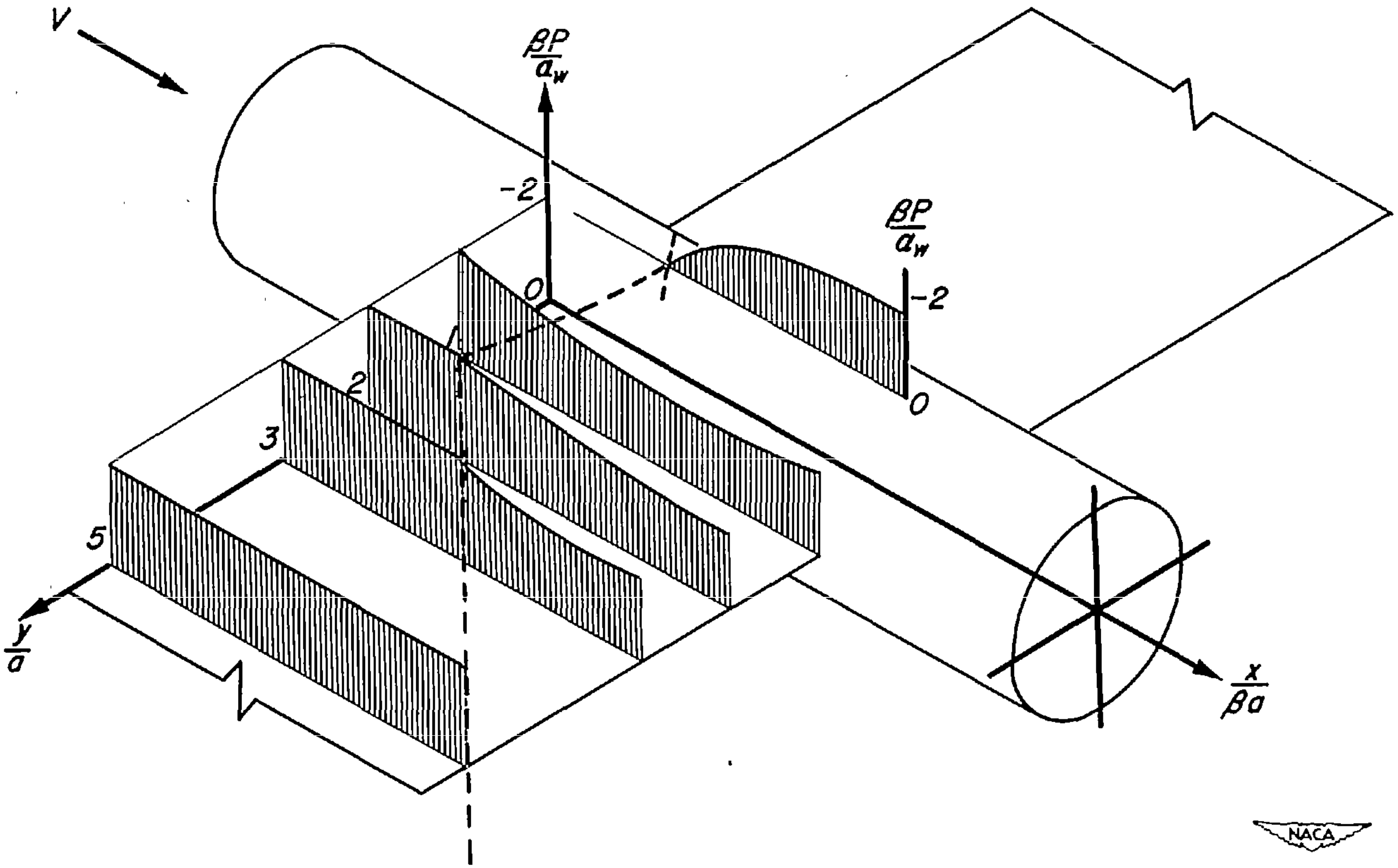
V
$\frac{\beta P}{a_w}$
-2
0
1
2
3
5
$\frac{y}{a}$
$\frac{\beta P}{a_w}$
-2
0
$\frac{x}{\beta a}$

Figure 19.- Isometric drawing of pressure distribution acting on combination of body and rectangular wing.

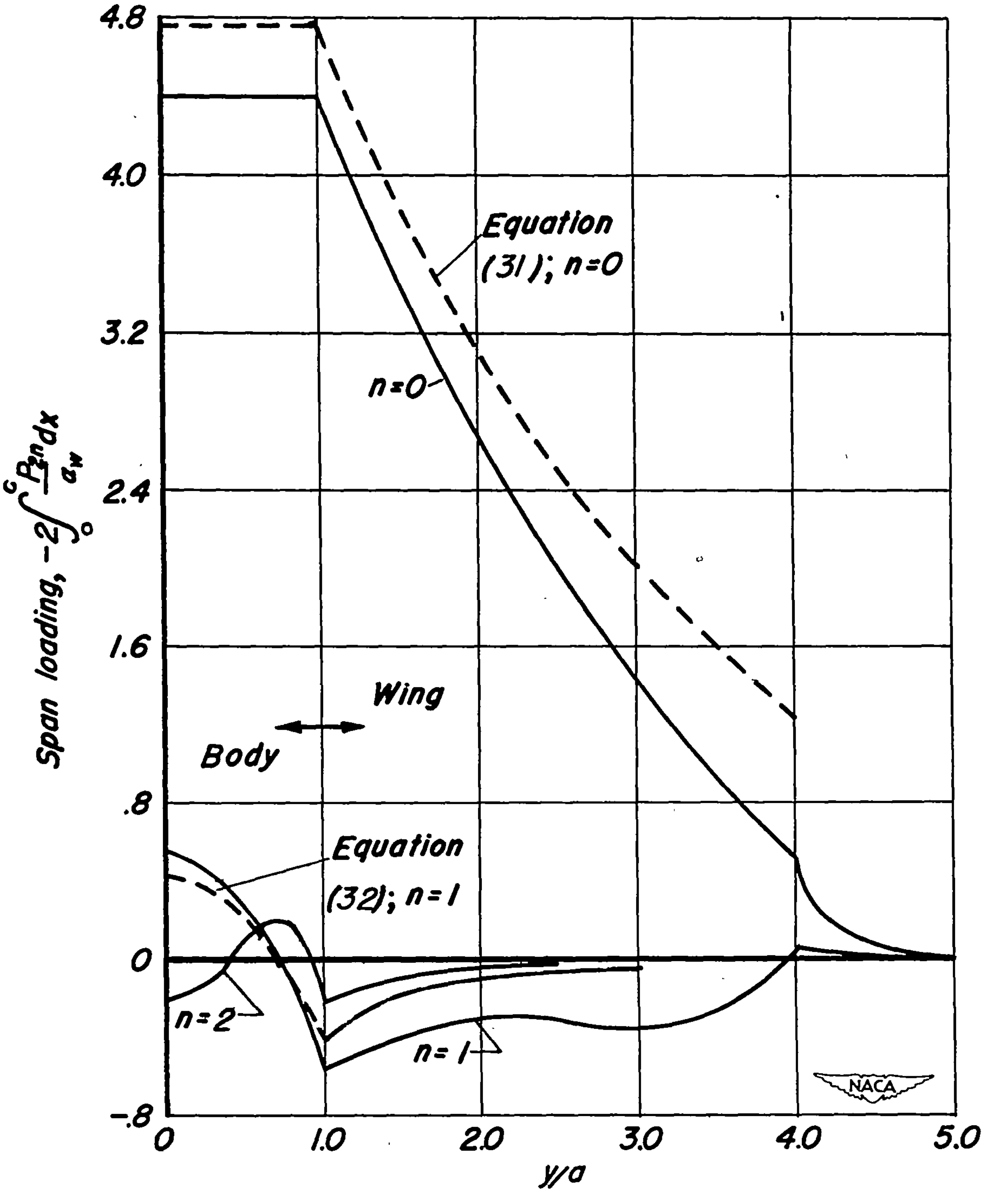

Figure 20.- Span loading of various Fourier components acting on combination of body and rectangular wing having effective chord-radius ratio of 4.

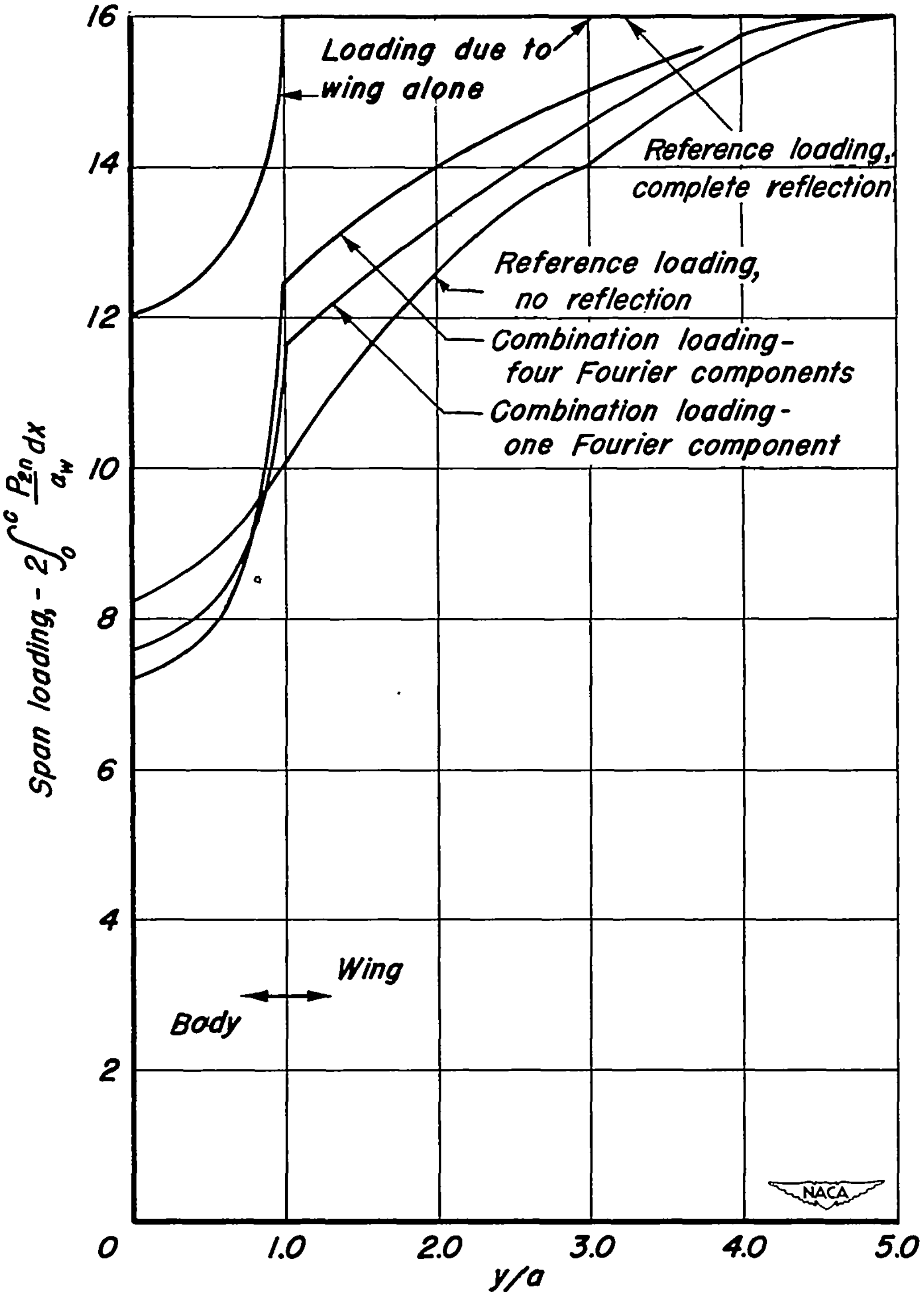

Figure 21.- Complete span loading for combination of body and rectangular wing having effective chord-radius ratio of 4.

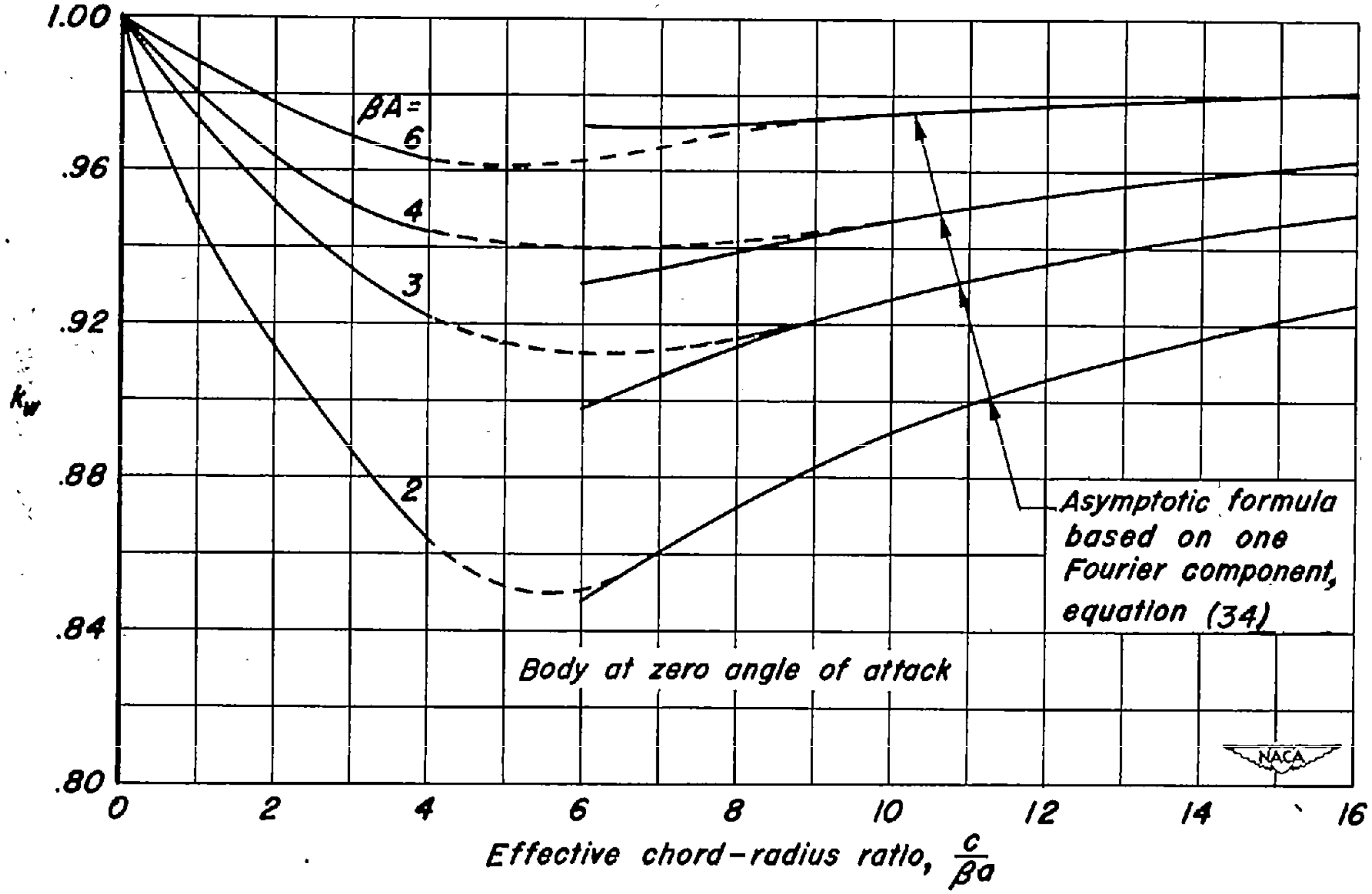

Figure 22.-Lift effectiveness for wing or control surface of combination of body and rectangular wing.

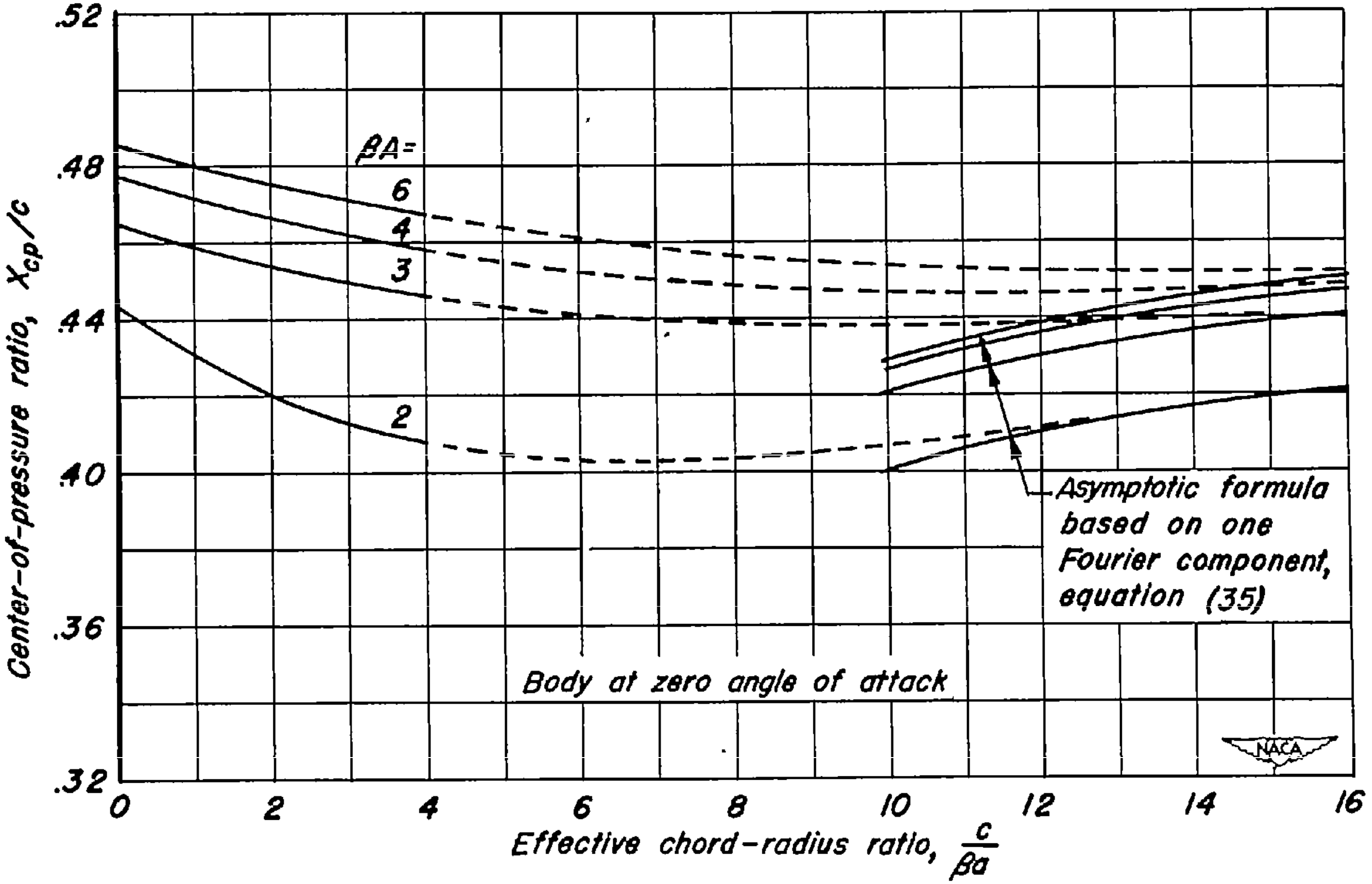

Figure 23.- Center of pressure for wing or control surface of combination of body and rectangular wing.

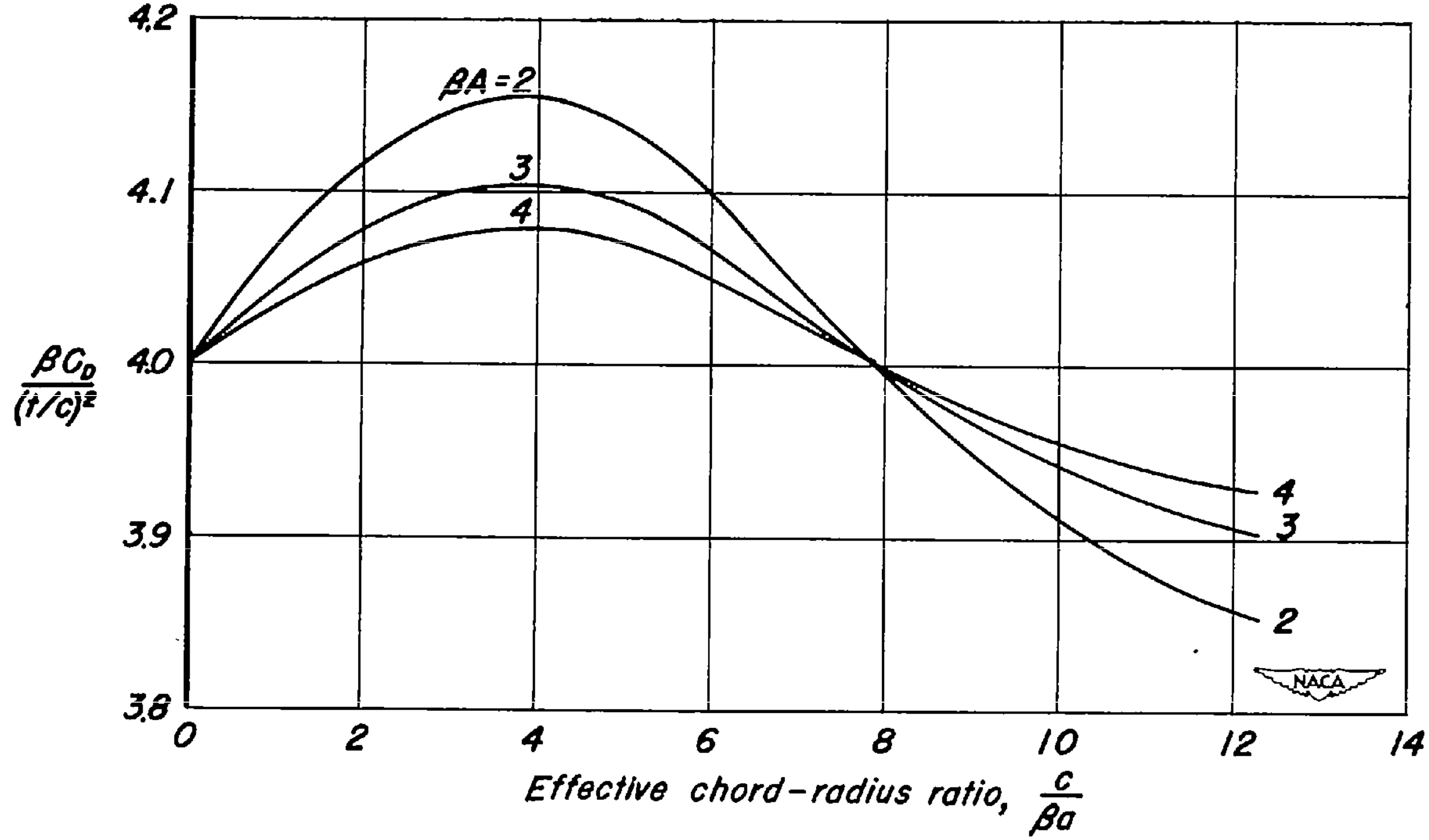

Figure 24.- Effect of interference on the minimum wave drag of a rectangular double-wedge wing mounted on a circular body, maximum thickness at wing midchord.

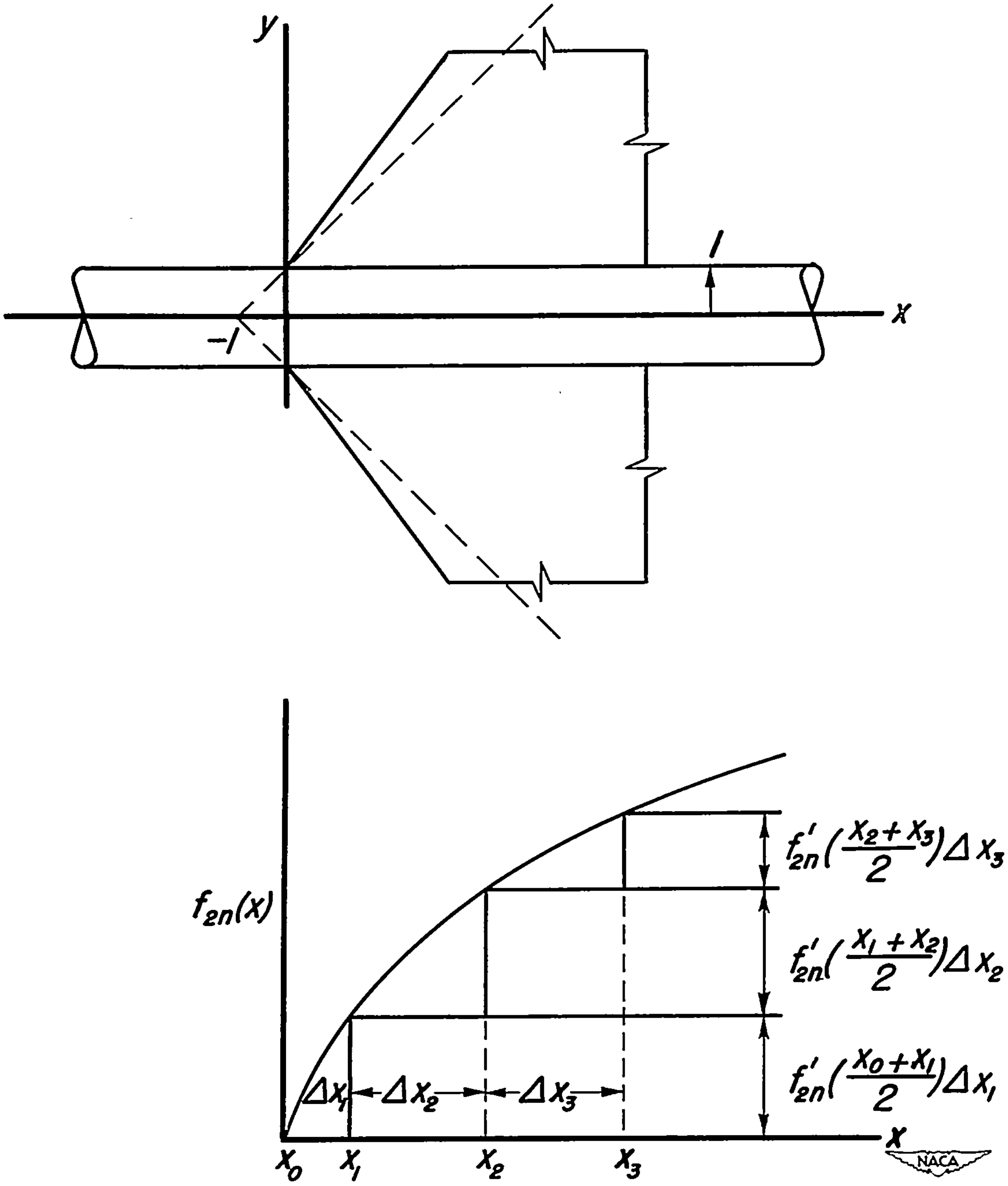
y
1
x
-1
$f_{2n}(x)$
$f'_{2n}(\frac{x_2+x_3}{2})\Delta x_3$
$f'_{2n}(\frac{x_1+x_2}{2})\Delta x_2$
$f'_{2n}(\frac{x_0+x_1}{2})\Delta x_1$
Δx_1
Δx_2
Δx_3
x_0
x_1
x_2
x_3
x

Figure 25.- Approximation of velocity amplitude function by series of step functions.

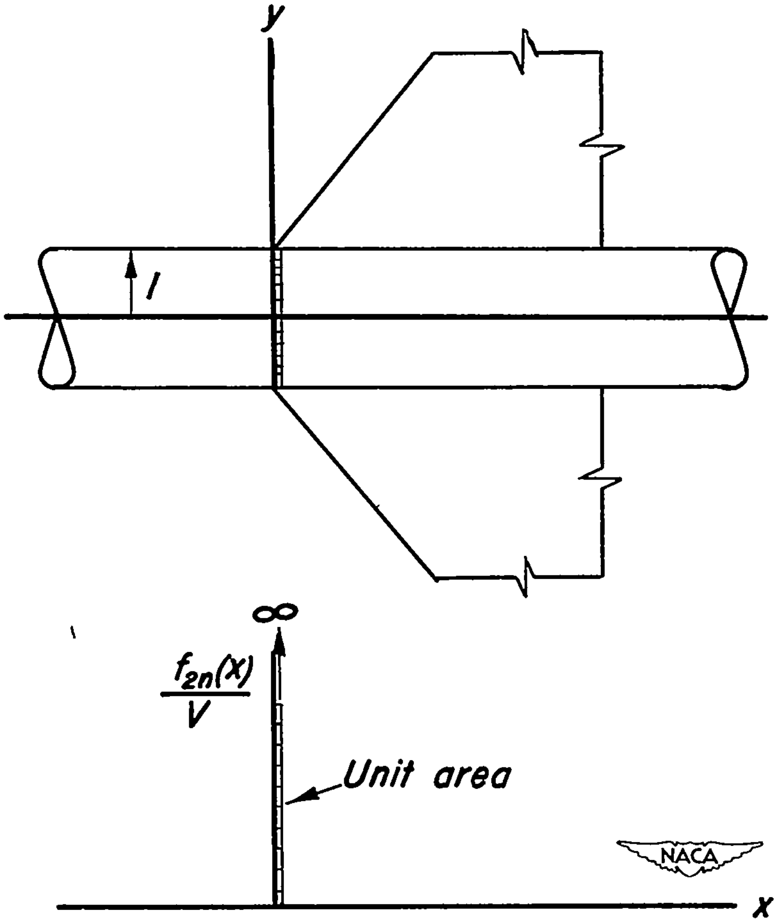
y
l
x
∞
$\frac{f_{2n}(x)}{V}$
Unit area
x

Figure 26.– Fourier component interference combination with "delta-function" protruberance at x = 0.

NACA-Langley - 4-16-52 - 1000